https://doi.org/10.5194/egusphere-2025-3919
Preprint. Discussion started: 21 August 2025

Very-High-Resolution, Multi-Season Monitoring of Crop Evapotranspiration and Water Stress with UAV Data and TSEB Integration

Jordan Steven Bates[1,2], Carsten Montzka[2], Harry Vereecken[2], François Jonard[1]

[1]Earth Observation and Ecosystem Modeling (EOSystM) Laboratory, SPHERES Research Unit, University of Liege, Liege, Belgium

[2]Institute of Bio- and Geosciences: Agrosphere (IBG-3), Forschungszentrum Jülich GmbH, 52428 Jülich, Germany

Correspondence to: Jordan Steven Bates (j.bates@uliege.be)

Abstract: Field-scale estimation of evapotranspiration (ET) using high-resolution data supports water conservation and yield optimization by enabling localized water use monitoring and early detection of crop stress. This study applies the Priestley–Taylor Two-Source Energy Balance (TSEB-PT) model at 15 cm resolution using unmanned aerial vehicle (UAV) data over a 10-hectare field across three seasons: sugar beet (2021), potato (2022), and winter wheat (2023). Key inputs included thermal infrared (TIR) for land surface temperature (LST), multispectral (MS) and LiDAR data for canopy characterization, and a fusion of MS derived green area index (GAI) and LiDAR derived plant area index (PAI) to derive the fraction of green LAI (f_g). Model outputs were validated against eddy covariance (EC) flux data using footprint modeling. Results showed high sensitivity to LST, emphasizing the importance of accurate thermal calibration. While both GAI and PAI provided comparable LAI inputs during peak growth, GAI better captured functional canopy decline during stress and senescence, especially in winter wheat, where dense structure led to cooling effects unrelated to transpiration. Dynamic f_g improved ET accuracy across all crops, particularly under declining canopy function. Overall, TSEB-PT showed strong agreement with EC measurements (RMSE = 0.14 mm/h, R^2 = 0.49; R^2 = 0.81 excluding senescence). UAV TIR based ET maps also revealed early stress signals prior to changes in MS or LiDAR based metrics. This study demonstrates the value of integrating very-high-resolution UAV data with the TSEB-PT model for multi-crop and season-long ET monitoring and early stress detection.

Keywords: UAS; Drone; Thermal-IR; LiDAR; Multi-sensor; Water use

https://doi.org/10.5194/egusphere-2025-3919
Preprint. Discussion started: 21 August 2025

1. Introduction

Evapotranspiration (ET), the combined loss of water through soil evaporation and plant transpiration, is the second-largest flux in the hydrological cycle after precipitation (Allen et al., 1998). ET plays a critical role in water resource allocation and irrigation scheduling (Wang et al., 2014). Plant health and biomass production is closely linked to transpiration, which depends on soil water availability and is regulated by stomatal and environmental conditions. Accurate, timely estimation of ET at the field scale is essential for optimizing irrigation schedules, improving water use efficiency (WUE) (Pereira & Pires, 2011), and supporting sustainable agriculture amid increasing water scarcity and climate variability (Colaizzi, 2016).

Conventional ET measurement methods, such as lysimeters, sap flow sensors, and eddy covariance (EC) systems (Yang et al., 2019), offer high temporal resolution but are limited in spatial coverage, making them inadequate for capturing within-field variability critical to precision irrigation Yao et al., 2017). Additionally, these systems are costly, making large-scale monitoring impractical (Yao et al., 2017). Satellite and airborne remote sensing approaches improve spatial coverage but often lack the resolution needed for dynamic crop monitoring. Manned aircraft, while capable of very-high-resolution observations, are costly and operationally demanding (Bellvert et al., 2020; Hunt Jr. & Daughtry, 2018).

Recent advances in unmanned aerial vehicles (UAV) and lightweight, very-high-resolution uncooled thermal infrared (TIR) sensors now enable on-demand, field-scale ET monitoring. UAV platforms offer both high spatial and temporal resolution, allowing for detailed detection of crop water stress and rapid changes in canopy function (Niu et al., 2020). TIR remote sensing in the 8–14 µm range is a key component of energy balance models, as land surface temperature (LST) serves as a direct proxy for canopy transpiration and stomatal regulation if crop aerodynamics are known (Tanner, 1963). Anderson et al. (2024) further reviewed the development of TIR based energy balance models, which link vertical temperature gradients to sensible heat flux by modeling resistance, surface, and vegetation interactions.

Popular and widely used models such as SEBAL and METRIC estimate ET using TIR derived LST and LAI data (Mohan et al., 2020), but their one-source energy balance formulations treat the land surface as a single layer. They rely on hot/cold (not transpiring/ fully transpiring) anchor pixels to infer ET extremes, with no explicit representation of soil–canopy interactions or functional canopy condition. This oversimplification can lead to inaccuracies (Niu et al., 2020), especially in heterogeneous or partially senescent fields, where vegetation structure and function vary spatially. However, even though these models are typically used with satellite based remote sensing, they have also been applied with UAV studies (Chandel et al., 2020; Mokhtari et al., 2021; Niu et al., 2019). Some UAV based studies have applied simplified alternatives such as the Deriving Atmosphere Turbulent Transport Useful To Dummies Using Temperature (DATTUTDUT) (Ellsäßer et al., 2020) or the Simple Algorithm for Evapotranspiration Retrieving (SAFER) (de Lima et al., 2024) but have similar constraints for very-high-resolution data at field scale.

Alternatively, Two-Source Energy Balance (TSEB) models partition energy fluxes between soil and vegetation, each with distinct resistances (Norman et al., 1995). It is considered one of the most robust and widely used (Nieto, 2022;

https://doi.org/10.5194/egusphere-2025-3919
Preprint. Discussion started: 21 August 2025

Nassar et al., 2020) while often outperforming OSEB models like SEBAL or METRIC when compared (Guzinski et al., 2020; Brenner et al., 2018; Jaafar et al., 2022; Tao et al., 2024; Xia et al., 2016) especially in variable and sparse vegetation cover (García-Santos et al., 2022; Derardja et al., 2024). There are several versions but the most commonly used is the Priestley-Taylor version (TSEB-PT) (Colaizzi et al., 2014). Additionally, TSEB-PT incorporates fraction of green LAI (f_g) within the Priestley-Taylor formulation which allows the model to dynamically scale transpiration based on the fraction of functioning canopy. This makes it especially suitable for modeling at high spatial resolution with heterogeneous canopy covers from partial stress and senescence conditions. Furthermore, TSEB-PT version avoids uncertainties tied to vapor pressure as opposed to the Penman–Monteith (TSEB-PM) version, which simplifies deployment for UAV based applications (Colaizzi et al., 2014). The TSEB-PT model has been used with several UAV crop studies including wheat (Gómez-Candón et al., 2021), Barley (Hoffmann et al., 2016); Sorghum (Tunca et al., 2023a), Pomegranate (Niu et al., 2019), but with most being vineyards (Gao et al., 2021, 2023; Nassar et al., 2020, 2021, 2022; Nieto et al., 2019; Ortiz et al., 2019; Xia et al., 2016).

Recently, machine learning (ML) methods have been applied to ET estimation using multispectral, thermal, and auxiliary data (Amani et al., 2023; Liyew et al., 2025). ML models often depend on large, high-quality ground data such as lysimeters (Kavya and Mahadevaiah et al., 2024) or eddy covariance systems (Liu et al., 2021), resources that are expensive, sparse, and highly site-specific, limiting their scalability for field-scale operational use (Hirschi et al., 2017) and are time consuming (García-Santos et al., 2022). Moreover, ML models struggle to transfer accurately to different locations or crop systems (Shi, 2024). In contrast, physically based models like TSEB-PT, when paired with UAV-sensor inputs, offer robust, interpretable, and transferable ET estimations across different crops and environments.

With these considerations in mind, we apply the TSEB-PT model for robust, multi-season UAV based ET estimation using very-high-resolution thermal infrared (TIR), multispectral (MS), and LiDAR data. However, small-uncooled TIR sensors are prone to radiometric drift and environmental noise, often requiring ground references to correct LST biases (Kelly et al., 2019). Modeling canopy resistance also hinges on reliable LAI estimates. MS derived green area index (GAI), which reflects pigment concentration, is widely used but susceptible to saturation in dense canopies (Bukowiecki et al., 2020; Zheng & Moskal, 2009). In contrast, LiDAR is increasingly being used for crop LAI type estimations (Bates et al., 2021; Hütt et al., 2022; Dreier et al., 2025). LiDAR derived plant area index (PAI) captures structural canopy density and reduces saturation-related errors (Bates et al., 2021; Ma et al., 2021). The fraction of green LAI (f_g), an indicator of photosynthetically active canopy, is rarely used in UAV based TSEB-PT studies. When included, it is typically assumed spatially constant (Hoffmann et al., 2016) or derived from sparse ground samples (Li et al., 2019) or NDVI based estimates, which lack structural depth (Nassar et al., 2022; Mendiguren et al., 2017). In this study, we leverage the complementary strengths of MS (GAI) and LiDAR (PAI) to generate dynamic, spatially explicit f_g estimates at pixel level. This has the potential to improved transpiration modeling that accounts for both canopy structure and physiological function.

https://doi.org/10.5194/egusphere-2025-3919
Preprint. Discussion started: 21 August 2025

Our study expands UAV based TSEB-PT modeling across three crop types, sugar beet, potato, and winter wheat, spanning full growing seasons, with validation against EC data. Beyond validation, we evaluate how the model captures field-scale ET variability and early signals of water stress. Specifically, we assess the sensitivity of ET to thermal calibration, compare GAI and PAI as LAI inputs, and test the impact of incorporating f_g derived from MS-LiDAR fusion. By testing these components under operational UAV conditions, this work advances the use of TSEB-PT for spatially adaptive, near real-time irrigation management in precision agriculture.

2. Methods

2.1. Study area

The study was conducted at the ICOS Class 1 ecosystem site DE-RuS within the TERENO Eifel Rur observatory in Selhausen, Germany (50°51′56″N, 6°27′03″E) (https://ddp.tereno.net/ddp/). The 10-hectare field is situated at 101–103 m above mean sea level with the soil consisting of Pleistocene loess, Holocene translocated loess, with sand and gravel at deeper levels (Brogi et al., 2020). The western section has shallower sand and gravel deposits, creating spatial variability in crop growth, especially during water-scarce periods. Weather conditions including precipitation and air temperature, during the experiment periods can be found in the appendix (see Tab. C1 & Fig. C6).

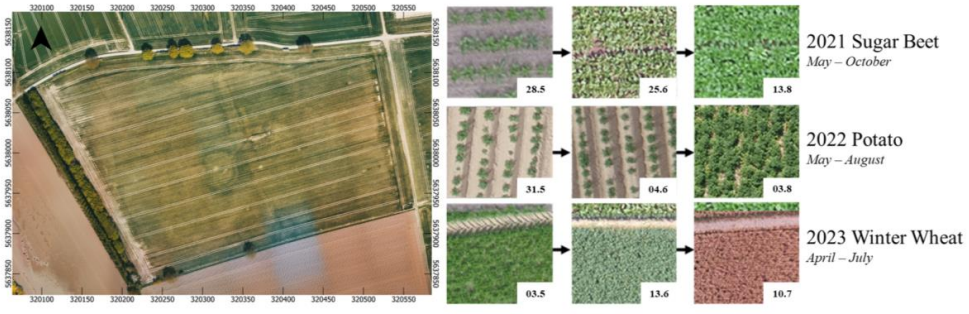

Figure 1: The field experiment site (left) with the EC and meteorological station located in the center of the field. The different crop cover type for each year (right) with example images of plant structure and fraction of vegetation coverage over the field throughout each growing season.

The field experiment site, shown in Fig. 1, was monitored over three growing seasons with different crops each year. In 2021, sugar beet was planted from May to October, starting with 20% vegetation cover and reaching 98% by harvest. In 2022, potatoes were grown from May to August, beginning with 5% cover and closing at 87%, with ridges between rows. In 2023, winter wheat was planted from April to July, maintaining 94-98% cover, with senescence marked by visible leaf browning. Only the potato crop was irrigated, receiving three 30 mm applications in July. These crop and soil variations provide a basis to evaluate the robustness of very-high-resolution UAV data in ET models like TSEB-PT.

2.2. UAV measurements and processing

https://doi.org/10.5194/egusphere-2025-3919
Preprint. Discussion started: 21 August 2025

Two DJI Matrice 600 UAV were used, one carrying a LiDAR payload and the other a combined MS and TIR setup (Fig. 2). The LiDAR system included a YellowScan Surveyor with a Velodyne VLP-16 scanner and Applanix APX15 GNSS-IMU, capturing 300,000 pulses/sec at 903 nm with ~4 cm precision. Flights were conducted at 50 m altitude and 8 m/s with 50% side overlap. A Septentrio Altus NR3 GNSS base station was used for georeferencing. LiDAR data were processed using POSPac (v8.6) and YellowScan's CloudStation.

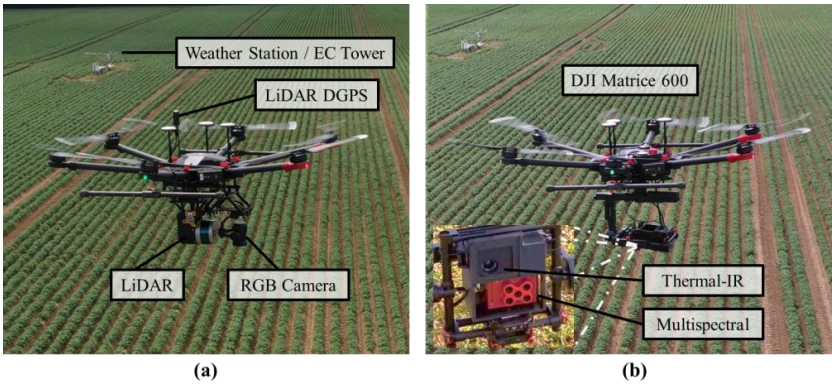

Figure 2: View of the DJI Matrice 600 UAV platforms that were used while flying over the field experiment site. (a) The M600 mounted with the YellowScan LiDAR Surveyor and DJI Zenmuse X1 RGB sensor. (b) The M600 with the FLIR Vue Pro R thermal IR modified with a ThermalCapture external heated shutter and Micasense Red-edge M multispectral sensors mounted on a 3-axis gyro system for nadir imagery.

The TIR sensor, a FLIR Vue Pro R 640 (13 mm), covered the 7.5–13.5 µm range with ±5°C accuracy and was modified with a heated shutter (ThermalCapture, AirRobot® GmbH & Co.) for improved inflight calibration. The MS sensor, a MicaSense RedEdge-M (AgEagle Aerial Systems Inc.), captured five spectral bands; red (663–673 nm) and NIR (820–860 nm) bands were used to calculate NDVI. Both sensors were mounted on a 3-axis gimbal and flown at 100 m altitude and 6 m/s, with approximately 90% image overlap. TIR calibration used internal corrections and ground temperature reference targets, while MS data were calibrated using a reflectance panel. Data from both platforms were processed in Pix4D. Flight campaign details are in the appendix (Tab. C1).

2.4. UAV data products and model implementation

TSEB-PT inputs fall into two categories: (1) surface boundary conditions derived from UAV data, including land surface temperature (LST), fractional vegetation cover (f_c), leaf area index (LAI), canopy height (h_c), and the fraction of green LAI (f_g); and (2) meteorological forcing variables, including air temperature (Ta), wind speed (u), vapor pressure (ea), and incoming solar radiation (Rn). UAV derived variables were processed and calibrated using ground measurements, with detailed methods outlined in Sections 2.4.1–2.4.5. Data processing and raster manipulation were conducted in RStudio using the raster and lidR packages. All datasets were resampled to a common 15 cm ground sampling distance (GSD). The full UAV processing and model integration workflow is illustrated in Fig. 3.

https://doi.org/10.5194/egusphere-2025-3919
Preprint. Discussion started: 21 August 2025

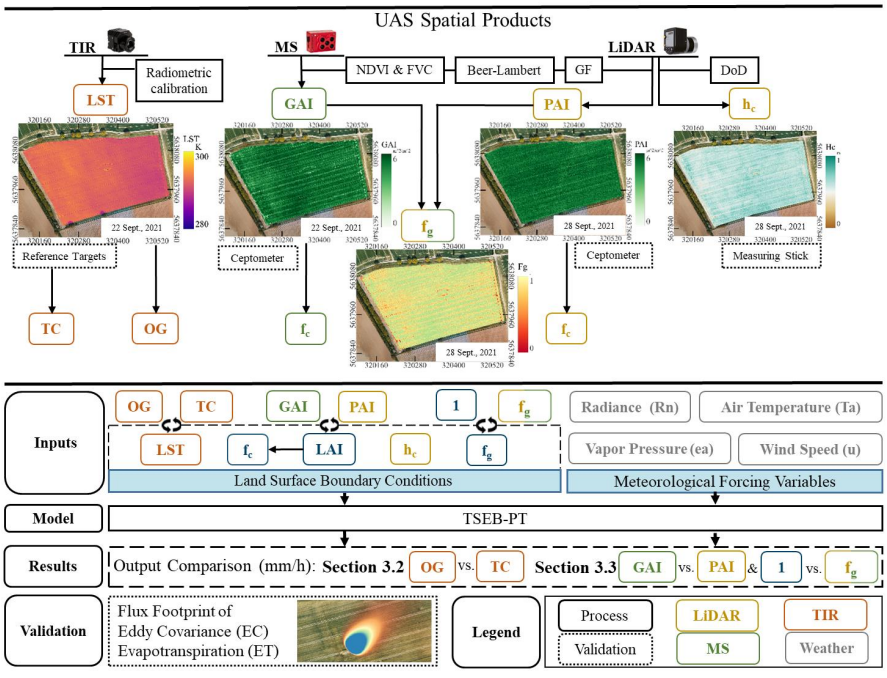

Figure 3: Workflow of the study, showing sensor data integration and input variations used in the TSEB-PT model. The model incorporates two categories of inputs: (1) surface boundary conditions and (2) meteorological forcing variables. Key UAV derived inputs, LST (original vs. corrected), LAI (LiDAR derived PAI vs. MS derived GAI), and f_g (default = 1 vs. UAV derived), were varied across model runs to assess their impact. Section 3.2 compares ET outputs using different LST inputs; Section 3.3 evaluates the influence of LAI source and the inclusion of f_g during senescence. Final ET estimates (mm/h) are validated against eddy covariance (EC) flux measurements within the modeled EC footprint area.

2.4.1. Land surface temperature (LST) maps

To convert incoming longwave radiance from the TIR microbolometers into LST, surface emissivity values were required. Constant emissivity values were assigned to each crop type based on a literature review. Although vegetation and bare soil exhibit different emissivity values, their differences were deemed negligible for the purposes of this study. Additional radiometric calibration parameters including air temperature, relative humidity, and the distance from the sensor to the target surface were input into the FLIR Vue Pro R sensor prior to each flight.

Uncooled thermal sensors on UAV platforms, such as the FLIR Vue Pro R, are prone to radiometric instability. This is largely due to inconsistencies in the default internal non-uniformity correction (NUC) applied to the microbolometer focal plane array. To improve calibration consistency, an external heated shutter was employed. Previous studies have reported that the use of such shutters can increase temperature measurement accuracy by up to 70% (Virtue et al., 2021). Another major source of radiometric noise arises from the sensor's own temperature and its interaction with the environment. Up to fourfold of the total signal noise can be attributed to sensor self-heating (Budzier & Gerlach,

https://doi.org/10.5194/egusphere-2025-3919
Preprint. Discussion started: 21 August 2025

2015; Gogler et al., 2014; Sagan et al., 2019). In addition, Kelly et al. (2019) demonstrated that wind exposure can destabilize sensor readings. To mitigate these effects, the thermal sensor was housed within a custom 3D-printed enclosure designed for thermal insulation and wind shielding. Furthermore, flights were conducted at reduced speeds to minimize wind-induced variability in sensor temperature.

Once radiometric calibration and sensor stability were addressed, LST accuracy was assessed using ground based reference targets. In the 2021 field season, a hot blackbody target (metallic surface) and a cold water body were deployed, and thermal images were captured before and after each flight at 100 meters AGL (Fig. C2). Notably, Virtue et al. (2021) reported that with the use of an external heated shutter, reference targets are no longer essential throughout the entire flight but just one reference image due to improved thermal stability. A consistent temperature offset was observed. To correct for this in subsequent seasons, a multiple linear regression model was developed using the 2021 reference data. This model incorporated environmental variables (wind speed, air temperature, and humidity) to generate corrected temperature offsets. Two types of LST inputs were ultimately used in the TSEB model: (1) the original temperature (OG), based solely on the sensor's internal radiometric calibration, and (2) the target-corrected temperature (TC), which applied the offset corrections derived from reference targets and the regression model.

2.4.2. Leaf area index (LAI)

Two types of LAI inputs were used in the TSEB-PT model: multispectral (MS) based green area index (GAI) and LiDAR based plant area index (PAI). GAI is derived from spectral reflectance and represents the photosynthetically active portion of the canopy (Park et al., 2021; Wei et al., 2023), while PAI is derived from LiDAR returns and reflects the total canopy structure, essentially independent of pigment content (Bates et al., 2021). Both metrics serve as proxies for LAI, before senescence onset, due to their established relationships with leaf biophysical traits (Tan et al., 2020; Ma et al., 2021).

GAI and PAI were calculated using a modified Beer–Lambert law, a widely used approach for modeling light attenuation in plant canopies (Ali et al., 2015; Thorp et al., 2010). GAI was estimated from MS derived fractional vegetation cover (FVC) (See Eq. B1 in appendix), while PAI was derived from LiDAR based gap fraction (GF) (See Eq. B3 in appendix). A commonly used pixel based approach was used to estimate FVC (Jia et al., 2017; Yue et al., 2021; Zhang et al., 2019). NDVI was applied to differentiate vegetation amounts and soil, with thresholds determined using NDVI histograms spanning the entire growing season. GF is defined as the proportion of laser pulses reaching the ground relative to total canopy returns within each raster cell. The extinction coefficient (k) was calibrated using proven (Oguntunde et al., 2012) in-field SunScan ceptometer LAI measurements and applied inversely to solve for GAI and PAI (see Eq. B2 & B4 in appendix B). Given limited ground samples per date (four CP zones), this semi-empirical method offered a balance with the limited ground LAI samples available.

Due to known variability in k across growth stages, especially during early canopy development, 2–3 k values were assigned per growing season, as recommended by Brogi et al. (2020) and Bates et al. (2021). Adjustments were

https://doi.org/10.5194/egusphere-2025-3919
Preprint. Discussion started: 21 August 2025

typically made after the first 2–3 sampling dates when canopy architecture changed rapidly. Thereafter, k was held constant through peak growth and harvest.

2.4.3. Fraction of green LAI (f_g)

To capitalize on the functional and structural canopy signals captured by GAI and PAI, we computed the fraction of green LAI (f_g), defined as the proportion of the total canopy (PAI) that remains photosynthetically active and capable of transpiring. f_g was calculated as the ratio of GAI to PAI:

$$f_g = GAI/PAI = \left(\frac{-log(1-FVC)}{k_{max}}\right)/\left(\frac{-\cos(\underline{\theta})\ln(GF)}{k_{max}}\right) \quad (1)$$

where $\underline{\theta}$ is the LiDAR scan angle, and k_{max} is the extinction coefficient derived from peak LAI prior to senescence. This formulation enables f_g to dynamically reflect changes in both pigment based canopy function and structural density.

The f_g input was set to 1 before senescence, assuming full canopy greenness and maximum transpiration capacity. After senescence onset, f_g values dropped based on relative differences between GAI and PAI, allowing the model to scale transpiration potential accordingly. Senescence timing varied by crop and was identified from field observations and GAI trends. For sugar beet (2021), senescence began after August 13 (three late-season dates); for potato (2022), after August 3 (one senescence date); and for winter wheat (2023), senescence onset was spatially variable and occurred as early as May 13, with six identified dates.

2.4.4. Fractional cover (f_c)

In TSEB-PT, f_c can be specified directly, however, when a LAI input is provided the model automatically computes f_c via the Beer–Lambert law (see Eq. A11 in appendix). This internal derivation maintains consistency in how net radiation is partitioned between soil and canopy, directly linking canopy area (whether structural or pigment-derived) to modeled fluxes. From the TSEB perspective, f_c should represent physical cover (Norman et al., 1995) as it governs canopy shading and soil radiation exposure which would best be based on structural LAI (PAI) as opposed to GAI. Therefore, in our f_g implementation we use PAI as the LAI input to ensure f_c better reflects actual canopy geometry and shading.

2.4.5. Crop height (h_c)

A method of difference of digital elevation models (DoD) was used to produce the h_c also commonly referred to as canopy height model (CHM) (see Eq. B5 in appendix B). A flight campaign was conducted before the emergence of the crops for a bare soil measurement to determine the digital terrain model (DTM_0). The remaining campaigns were those with crop surface structures to derive the digital surface model (DSM_d) for that particular campaign date. Having bare soil terrain data rather than using the ground points of the LiDAR for each campaign is better in decreasing

https://doi.org/10.5194/egusphere-2025-3919
Preprint. Discussion started: 21 August 2025

needed interpolations that would decrease the overall accuracy (Cao et al., 2019). The maximum values per pixel were taken when subtracting the DTM_0 from the DSM_d.

2.4.6 TSEB-PT model and contributions of UAV Derived Inputs

The TSEB-PT model partitions net radiation (Rn) into latent (LE), sensible (H), and ground (G) heat fluxes, with LE converted to evapotranspiration (ET, mm/h). The model was implemented using the pyTSEB library (Nieto et al., 2018). Figure 4 and Table 1 illustrate how each UAV derived variable informs distinct model components and their representation of surface–atmosphere interactions. Model equations are detailed in Eq. A1–A13 in the appendix and Norman et al., (1995).

Table 1: UAV derived model inputs, their influences within the model, and equation with which they are used.

UAV Input	Role in Model	Equation(s)
Surface temperature (T_c,T_s)	Drives partitioning and energy balance	A5, A6, A10
Fractional cover (f_c)	Radiative separation of canopy/soil temps	A10
Leaf Area Index (LAI)	Canopy resistance and transpiration estimation	A8, A11
Green LAI fraction (f_g)	Controls LE_c in Priestley–Taylor term	A11
Crop height (h_c)	Aerodynamic roughness estimation	A8, A9 (via d_0, z_0)

LST is a primary driver of H, representing the radiometric temperature of the combined canopy and soil surface. In vegetated areas, it influences aerodynamic surface temperature and temperature gradients critical for energy balance closure. LST, in conjunction with vapor pressure deficit (VPD), helps detect plant water stress, elevated LST and low transpiration under high VPD suggest stress. The f_c partitions energy fluxes between soil and vegetation. Higher f_c increases the canopy's contribution to Rn and LE, thus generally elevating ET while reducing G and H_s.

The LAI input, MS-GAI or LiDAR-PAI in this use case, affects aerodynamic (R_a) and canopy (R_x) resistances; higher LAI (more stomata) reduces R_x enhancing transpiration and LE. The f_g input captures the proportion of active vegetation within the structural LAI. It adjusts the Priestley-Taylor coefficient (α_PT) to reduce LE estimates during senescence or stress, preventing overestimation of transpiration. This is especially relevant in dense and tall crops, where inner canopy cooling can be misattributed to transpiration without accurate f_g representation (Elfarkh et al., 2020; Kustas et al., 2016).

The h_c input influences R_a by determining surface roughness (z_o) and displacement height (d), key variables for modeling turbulent heat exchange with the atmosphere. Taller canopies enhance aerodynamic coupling and energy dissipation, favoring higher ET. In contrast, shorter vegetation limits this exchange, increasing sensible heat flux (H) and reducing evaporative cooling. Also, h_c indirectly affects R_x, for defining boundary-layer development and vertical wind attenuation.

https://doi.org/10.5194/egusphere-2025-3919
Preprint. Discussion started: 21 August 2025

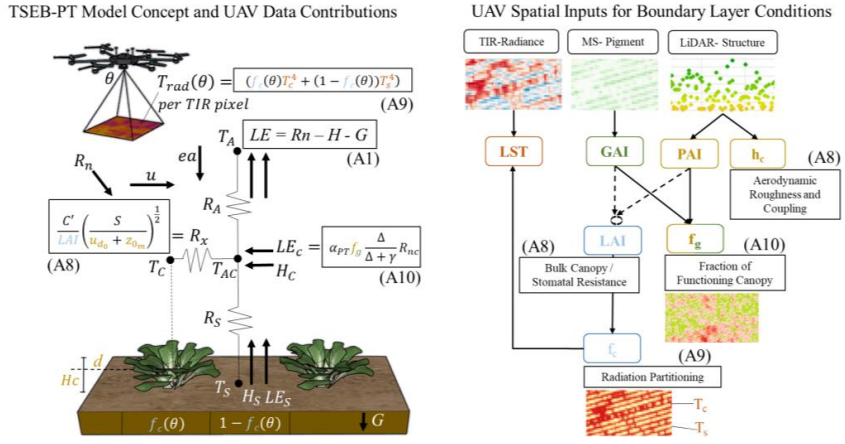

Figure 4: Schematic and data illustration of UAV derived inputs used in the TSEB-PT model. The left panel shows the model architecture, highlighting the partitioning of net radiation (Rn) into latent (LE), sensible (H), and ground (G) heat fluxes, and how UAV derived variables (color coded) influence each component. Key inputs include land surface temperature (LST), leaf area index (LAI), fraction of green LAI (f_g), fractional vegetation cover (f_c), and canopy height (h_c). The right panel displays spatial maps of LST, f_c, GAI, PAI, and f_g, along with a sample transect of the LiDAR 3D point cloud used to derive h_c and PAI. Data are shown for a sugar beet field, illustrating seasonal transitions in vegetation structure and function. Together, these inputs improve spatially explicit energy balance partitioning and ET estimation, particularly under variable vegetation conditions, such as during senescence. Abbreviations: R_a (s/m): aerodynamic resistance; R_x (s/m): canopy (bulk stomatal) resistance; R_s (s/m): soil resistance; T_c (K): canopy temperature; T_s (K): soil surface temperature; u (m/s): wind speed; ea (kPa): actual vapor pressure; z_0 (m): surface roughness length; d (m): zero-plane displacement height; α_PT (–): Priestley–Taylor coefficient (modified here by f_g); LE_c, H_c (W/m^2): Component fluxes from canopy; LE_s, H_s (W/m^2): Component fluxes from soil.

2.4.7 Weather station, EC ET, and flux footprints validations

Ground measurements were obtained from various instruments to support UAV data validation and model calibration. EC flux data, processed according to ICOS standards, were used to validate UAV derived ET estimates. EC measurements, including wind speed, direction, and water vapor concentration, were used to compute vertical fluxes related to ET (Ghiat et al., 2021). The footprint of the EC flux station was estimated using the footprint prediction model (FPP) in RStudio (Kljun et al., 2015), which accounts for micro-meteorological conditions and surface roughness. These footprints were calculated in correspondence within the duration of each UAV flight. UAV based TSEB-PT evapotranspiration (ET) estimates were compared to eddy covariance (EC) measurements by extracting the weighted average of raster pixel values within the 90% flux footprint extent. Each flux footprint can be seen in Appendix C with Fig. C1.

3. Results

3.1. UAV data derived model inputs

https://doi.org/10.5194/egusphere-2025-3919
Preprint. Discussion started: 21 August 2025

The thermal infrared (TIR) data collected by the UAV consistently underestimated ground surface temperature when compared to in-field reference targets during the 2021 season. The uncorrected TIR data showed a mean RMSE of 4.19 °C relative to thermometer readings but maintained strong agreement in relative temperature patterns across dates (R^2 = 0.97). After applying corrections using ground reference targets, the seasonal RMSE improved to 2.78 °C. Sensor offset (RMSE) was most strongly correlated with increased air temperature (0.74), followed by higher wind speed (0.55) and denser humidity (0.34). Based on these relationships, a multiple linear regression model was developed to predict and correct TIR sensor bias. This model was applied to subsequent field seasons, resulting in an average increase of 2.2 °C in the LST orthomosaics to improve temporal consistency across acquisition dates. These shifts in LST values before and after correction are illustrated in Fig. 5.

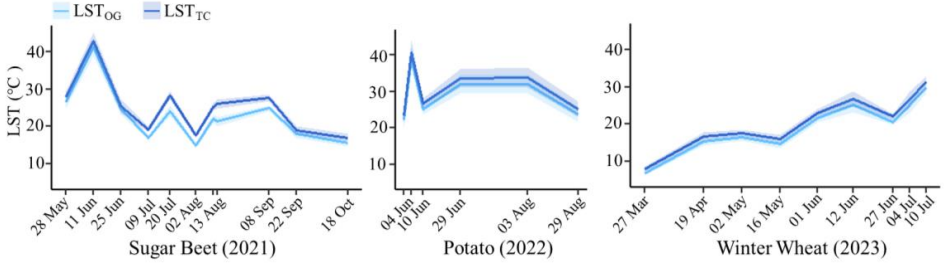

Figure 5: (a) The comparison of UAV average temperatures of the ground targets as compared to the average of the recorded temperatures of the thermometers. (b) Correlation of weather conditions with the difference (delta) between the thermal sensor and actual temperature of ground thermal targets for each date.

For LAI estimation, both multispectral derived green area index (GAI) and LiDAR derived plant area index (PAI) were evaluated against ground based ceptometer LAI measurements. Across all three crops, PAI estimates were consistently more accurate, with lower RMSE values and higher correlation to field observations. Specifically, PAI achieved R^2 values of 0.99 for all three crops and an overall RMSE of 0.27 m^2/m^2, whereas GAI showed greater variability, especially in winter wheat, resulting in an overall RMSE of 1.02 m^2/m^2 and R^2 of 0.88. The discrepancy between GAI and PAI was most evident during senescence, when chlorophyll degradation reduced the spectral signal used in GAI estimation, while LiDAR still captured high canopy structural density. These results highlight the functional–structural divergence between optical and structural measurements of LAI, especially under changing vegetation conditions. A comparison of GAI and PAI estimates against ground LAI measurements at the field scale is shown in Fig. 6.

https://doi.org/10.5194/egusphere-2025-3919
Preprint. Discussion started: 21 August 2025

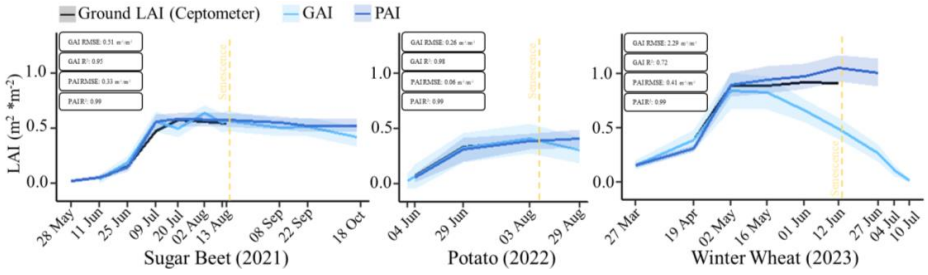

Figure 6: Field averaged UAV derived green area index (GAI) and plant area index (PAI) compared to ground based ceptometer LAI measurements across each campaign for three growing seasons. Ground measurements conclude prior to the onset of senescence, during which divergence between GAI and PAI becomes more pronounced due to declining pigment content in the canopy.

UAV derived canopy height (h_c) showed strong agreement with ground based measuring stick observations across all crops. In the 2023 winter wheat season, where canopy structure was most uniform, h_c estimation achieved excellent accuracy (RMSE = 0.01 m, R^2 = 0.99). Lower accuracy was observed in potato (RMSE = 0.12 m), likely due to the effects of ridge planting and heterogeneous canopy closure within sampled areas. Despite this, the UAV LiDAR system provided reliable height estimates across all crops, with an overall RMSE of 0.06 m and R^2 = 0.90. These results support the suitability of UAV based h_c for use in aerodynamic roughness parameterization within the TSEB-PT model. A comparison of UAV derived and ground measured canopy heights is shown in Fig. 7.

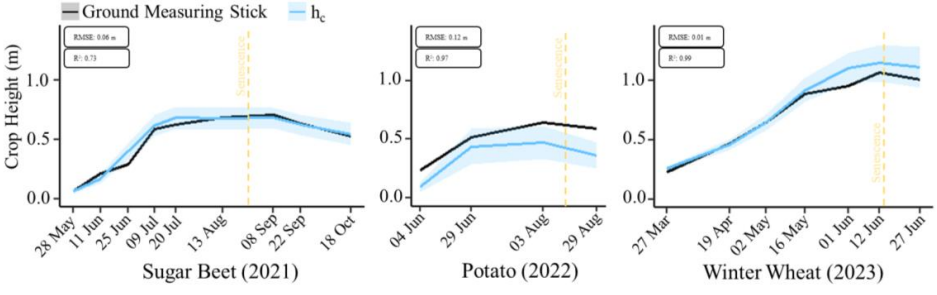

Figure 7: Comparison of UAV LiDAR derived canopy height (h_c) and ground based measuring stick data for each season. UAV derived values represent field wide averages, while ground measurements reflect averages within designated control point (CP) zones.

3.2. Accuracy and sensitivity of TSEB-PT ET estimates from UAV thermal corrections

To assess the impact of radiometric calibration on ET model performance, we compared TSEB-PT estimates derived from original (LST_{OG}) and target corrected (LST_{TC}) UAV thermal imagery against EC derived ET values across all three crop seasons as seen in Fig. 8.

https://doi.org/10.5194/egusphere-2025-3919
Preprint. Discussion started: 21 August 2025

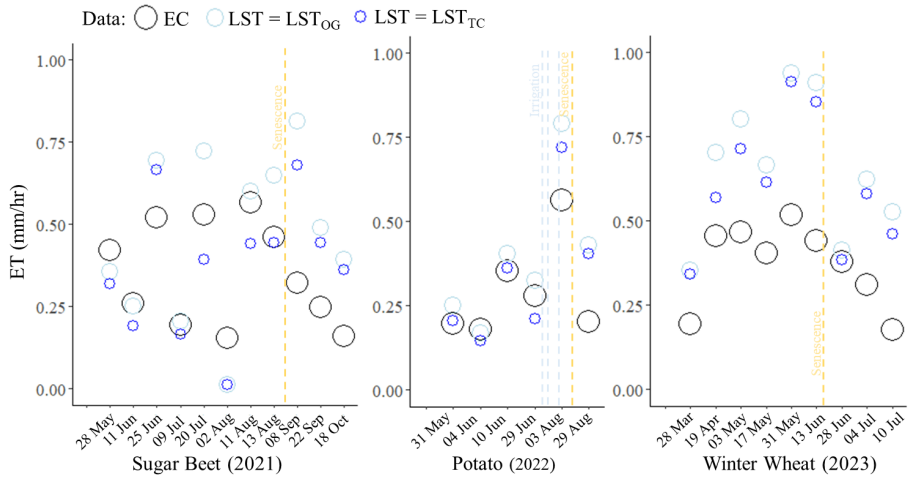

Figure 8: Comparison of UAV derived TSEB-PT ET estimates for each season using two different TIR inputs: uncorrected original (OG) and target corrected (TC) LST data. ET outputs are compared against eddy covariance (EC) measurements within the corresponding flux footprint for each campaign.

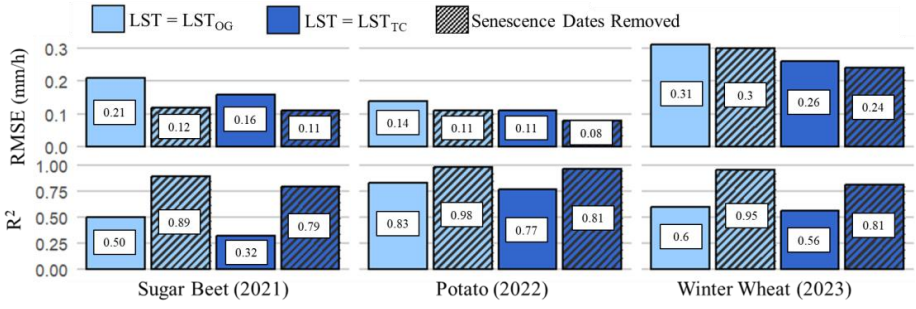

Figure 9: RMSE and R² between modeled TSEB-PT ET and EC derived ET, averaged over the EC flux footprint. Two TSEB-PT model runs are compared based on land surface temperature (LST) input: original (OG) and target corrected (TC). Statistical metrics are presented for the entire growing season and excluding senescence periods, highlighting the influence of canopy condition on model performance.

Referring to Fig. 9, across all three crops, the use of target corrected LST (LST$_{TC}$) inputs reduced overall RMSE, indicating improved absolute agreement between TSEB-PT ET estimates and EC observations. For example, both sugar beet and winter wheat showed seasonal RMSE reductions of approximately 0.5 mm/h. However, while thermal correction enhanced the absolute accuracy of LST and the resulting ET values, it also introduced temporal smoothing, which in some cases reduced the model's sensitivity to short-term variability. This was most evident in the 2021 sugar beet season, where R^2 declined from 0.50 (LST$_{OG}$) to 0.32 (LST$_{TC}$) despite improved RMSE. Although R^2 decreased slightly, the improved thermal realism from corrected LST values enhances the physical accuracy of ET estimates.

In all three crop seasons, omitting campaign dates during crop senescence, showed that the model estimations performed significantly better before physiological decline of the crops. The most pronounced improvement was

https://doi.org/10.5194/egusphere-2025-3919
Preprint. Discussion started: 21 August 2025

observed in sugar beet, where RMSE decreased from 0.16 to 0.11 mm/h and R^2 increased from 0.32 to 0.79 when using LST_{TC}.

3.3. Accuracy and sensitivity of TSEB-PT ET estimations from different UAV based LAI inputs

Building on the thermal correction analysis, we next evaluated how the choice of LAI input, multispectral derived GAI versus LiDAR derived PAI, influences TSEB-PT ET estimates as seen in Fig 10. In addition, we used GAI/PAI to compute the fraction of green LAI (f_g), allowing dynamic scaling of the Priestley–Taylor coefficient (α_PT) to account for senescence or stressed vegetation. Model runs using f_g were compared to a baseline with no scaling of α_PT (i.e., assuming $f_g = 1$), to assess their impact on ET estimates under varying canopy conditions.

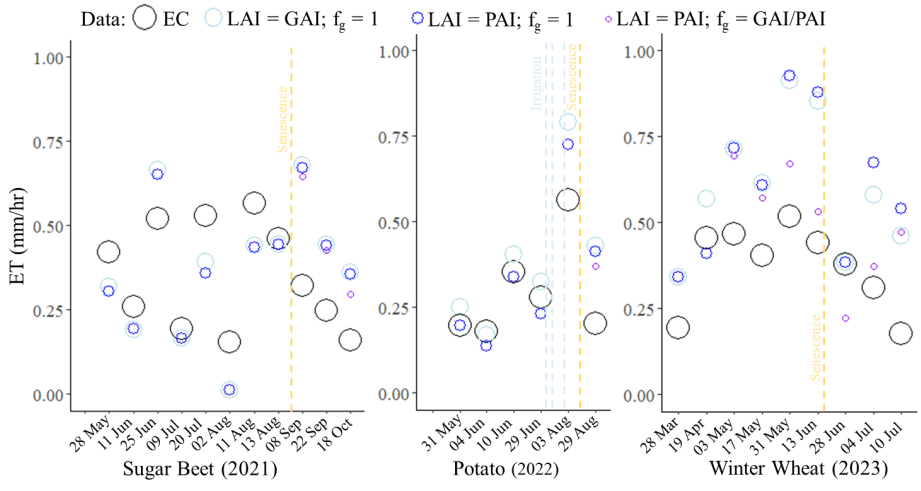

Figure 10: TSEB-PT evapotranspiration (ET) estimates were evaluated using different leaf area index (LAI) inputs: MS derived green area index (GAI), LiDAR derived plant area index (PAI), and their ratio, representing the fraction of green LAI (f_g), during periods of known senescence. UAV derived ET was compared against eddy covariance (EC) measurements within the EC flux footprint to assess model sensitivity to LAI input type. Notably, f_g scaling was introduced earlier for winter wheat in the model than the officially declared onset of senescence to account for localized early decline observed in the western portion of the field due to water deficits.

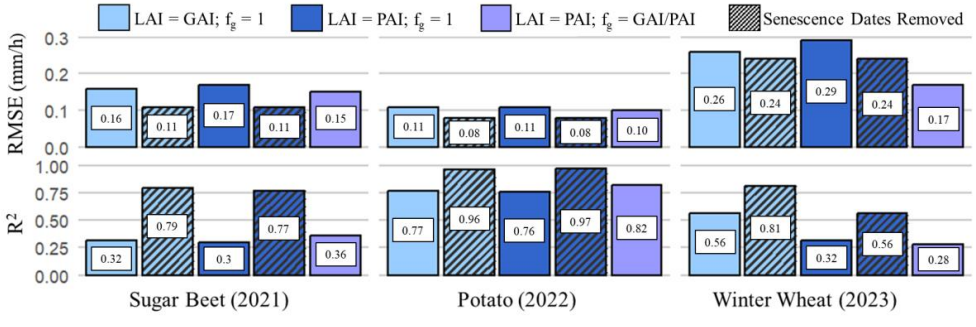

https://doi.org/10.5194/egusphere-2025-3919
Preprint. Discussion started: 21 August 2025

Figure 11: RMSE and R^2 between TSEB-PT modeled ET and EC derived ET, averaged over the EC flux footprint. Two different LAI inputs were evaluated: green area index (GAI) and plant area index (PAI). Statistical metrics are shown for all campaign dates and separately for dates excluding senescence. During senescence periods, a third approach using the fraction of green LAI (f_g = GAI/PAI) was also evaluated to scale transpiration according to functional canopy condition.

During early to mid-season growth, when canopies were predominantly green and structurally uniform, the choice of LAI input, GAI or PAI, had minimal effect on model performance. Excluding senescent dates, ET estimates from both types of LAI inputs were in close agreement with EC measurements across all three crops. Coefficients of determination (R^2) were also similar, with the exception of winter wheat, where GAI yielded a noticeably higher R^2 despite equivalent RMSE.

However, during senescence, discrepancies between GAI and PAI based LAI inputs became more pronounced, particularly in winter wheat. While PAI values remained elevated due to the persistence of canopy structure, GAI declined in response to chlorophyll degradation as seen in Fig. 6. These differences had a notable impact on model accuracy over the whole growing season of winter winter wheat, where LAI = PAI estimates exhibited a higher overestimation with a RMSE of 0.29 mm/h and lower R^2 (0.32), while LAI = GAI inputs improved performance with an RMSE of 0.26 mm/h and R^2 of 0.56.

Incorporating f_g significantly reduced ET overestimation during senescence and improved agreement with EC measurements in every season. Because of the significant and early physiological decline in in winter wheat, these improvements were even more significant. In winter wheat the RMSE decreased from 0.29 mm/h with LAI = PAI and f_g = 1 to 0.17 mm/h LAI = PAI and f_g = GAI/PAI.

3.4. Input impacts on resulting magnitude of ET map spatial variability

This study revealed that TSEB-PT derived ET with very-high-resolution data varied with both magnitude and spatial distribution across campaign dates influenced by the choice of UAV derived inputs. Appendix Figures B10 and B11 present field averaged ET values along with their standard deviations, demonstrating how input configurations affect field spatial variability in modeled ET. To explore the sensitivity of ET spatial variability to input differences, we analyzed the changes in the coefficient of variation (CV) of ET in response to modifications in key model inputs. Specifically, Figure 12 shows how ET CV responds to the differences in input CV for LST (TIR_{OG} CV – TIR_{TC} CV), LAI sources (GAI CV – PAI CV), and f_g (f_g = 1 CV - GAI/PAI derived f_g CV). These comparisons help establish the connection between input variability and the spatial behavior of ET estimates, providing insight into which inputs most strongly influence the spatial characteristics of TSEB-PT outputs across varying crop and environmental conditions.

https://doi.org/10.5194/egusphere-2025-3919
Preprint. Discussion started: 21 August 2025

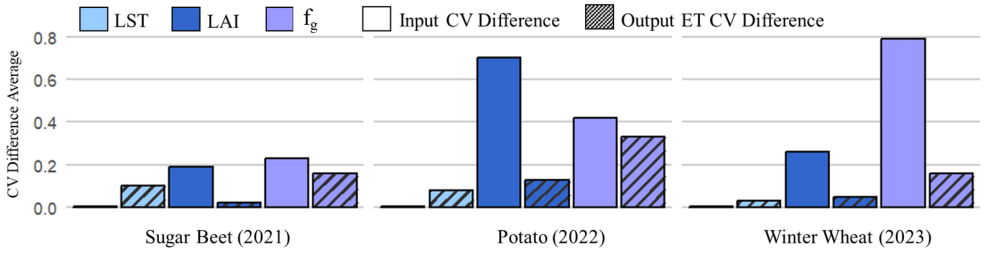

Figure 12: Comparison of average differences in the coefficient of variation (CV) between key TSEB-PT input variables (LST, LAI, f_g) and the resulting ET estimates across three crop types. This highlights how changes in the spatial variability of each input affect the spatial variability of modeled ET. The CV difference for f_g reflects the transition from a uniform value (f_g = 1) to a spatially variable product derived from the fusion of GAI and PAI.

Notably, with a uniform increase in average LST resulted in significant shifts in the spatial distribution of TSEB-PT ET estimates. In contrast, despite greater coefficient of variation (CV) between MS derived GAI and LiDAR derived PAI inputs, their influence on ET spatial variability was comparatively limited. The incorporation of a dynamic f_g, derived from the fusion of GAI and PAI, substantially altered the spatial representation of ET, underscoring the importance of this parameter.

Given the substantial change in ET spatial variability resulting from an essentially uniform shift in LST inputs, we further examined the corresponding ET maps for potato in early season (low vegetation cover) and late season maps (variability in vegetation state). This was to characterize the different spatial magnitudes of ET change were spatially distributed with uniforms shifts in LST. These comparisons are presented in Fig. 13 where the LST_{OG} ET (lower LST and higher resulting ET) results were subtracted from those when LST_{TC} inputs were used.

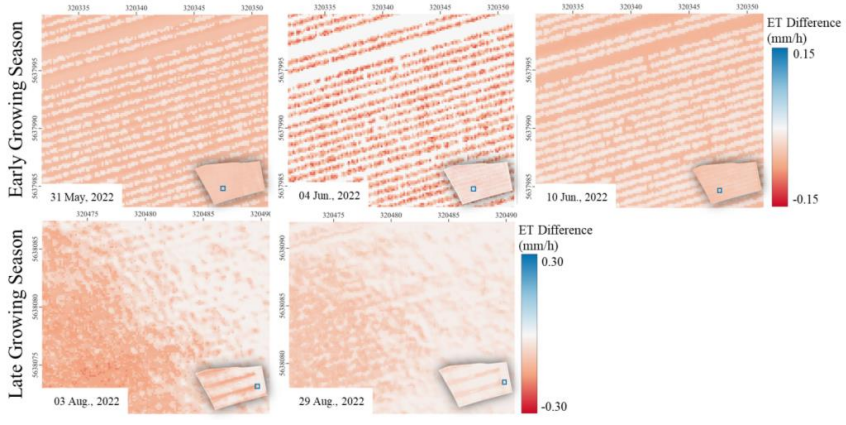

Figure 13: Difference in TSEB-PT ET estimates using original land surface temperature (LST_{OG}) ET minus reference target corrected (LST_{TC}) ET. The maps illustrate how the magnitude and spatial pattern of ET differences vary depending on the dominant evaporative source (soil vs. canopy) and the presence of crop water stress.

https://doi.org/10.5194/egusphere-2025-3919
Preprint. Discussion started: 21 August 2025

Two key characteristics on how increased LST offset changes spatial variability in TSEB-PT ET outputs were observed. First, in early-season conditions with lower f_c, the dominant flux, whether from soil evaporation or canopy transpiration varied across dates and increased the contrast between soil and canopy with the increased temperature from LST_{TC}. Second, later in the growing season, the magnitude of ET change differed significantly depending on presence of stressed vegetation. In these cases, stressed vegetation showed a substantially larger ET reduction after LST correction. This shows thermal correction reshaped the spatial structure of modeled water use, amplifying contrasts between stressed and non-stressed zones.

3.5. Precise early identification of crop water stress with high-res ET maps

One of the most practical advantages of TIR based UAV derived ET modeling is its capacity to detect early signals of crop water stress before structural or spectral changes manifest in traditional vegetation indices. In the 2022 potato and 2023 winter wheat seasons, this capability was clearly demonstrated as seen in Fig. 14 & 15.

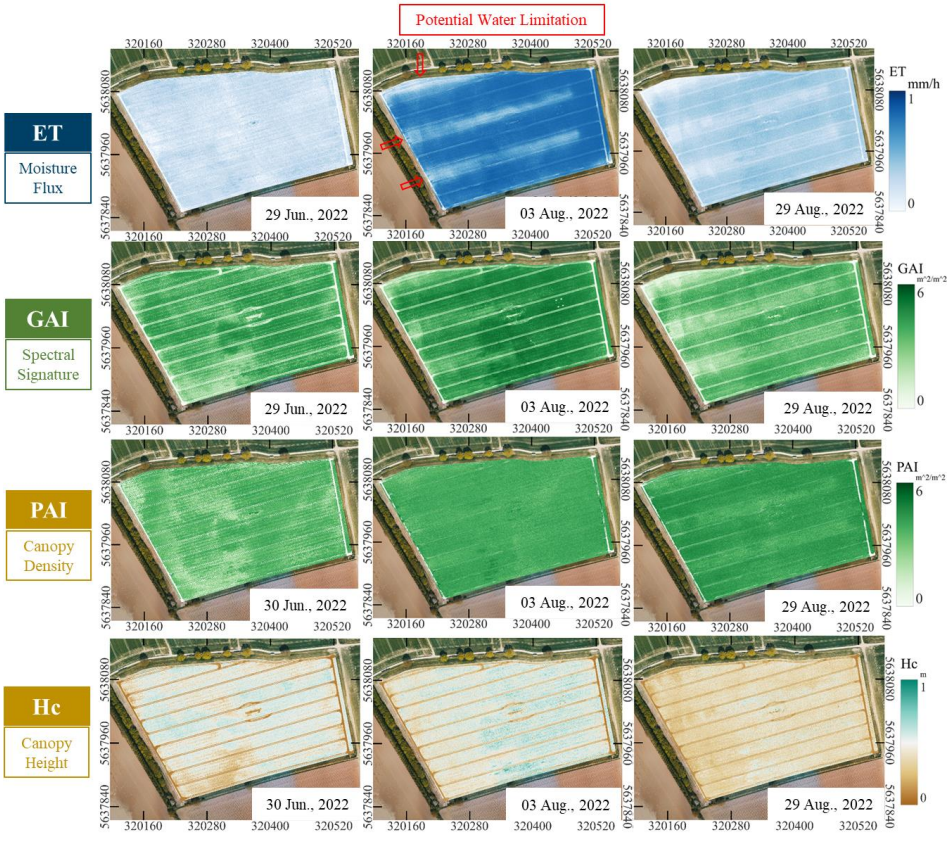

Figure 14: Particular dates in the potato 2022 season of Evapotranspiration (ET), green area index (GAI), plant area index (PAI) comparisons around moments of potential water related stress. ET map shows clear structures within field related

https://doi.org/10.5194/egusphere-2025-3919
Preprint. Discussion started: 21 August 2025

to irrigation patterns on the 3rd of August more so than with GAI and PAI. On the 29th of August, consequences in pigment and canopy structure can be seen with GAI and PAI.

Comparisons between the August 3 and August 29 UAV campaigns in 2022 revealed that, despite minimal changes in both GAI and PAI, the ET maps captured pronounced declines in water use across specific sections of the field. These reductions aligned with known zones of reduced irrigation coverage caused by limitations of the hose reel sprinkler system. Notably, areas along the northwest corner and adjacent to irrigation lanes exhibited significant ET suppression, even though they remained structurally intact in LiDAR and multispectral imagery.

A similar pattern was observed in 2023 with winter wheat, though in this case the stress was most likely attributed to known underlying soil–root interactions that have caused water stress in the past. On June 13, the ET map revealed broader and more pronounced spatial structures of suppressed transpiration that were not yet visible in the GAI or PAI maps. By June 28, however, similar spatial patterns emerged in both GAI and PAI, confirming physiological and structural canopy decline.

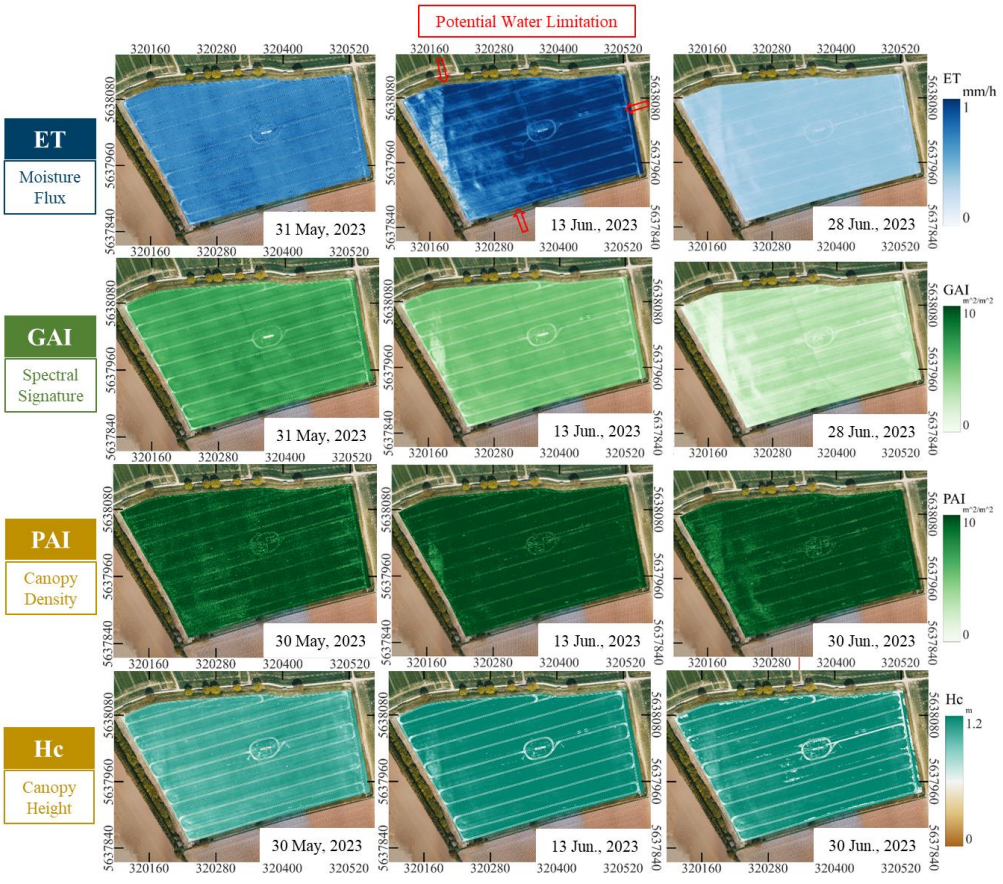

https://doi.org/10.5194/egusphere-2025-3919
Preprint. Discussion started: 21 August 2025

Figure 15: Particular dates in the winter wheat 2023 season of Evapotranspiration (ET), green area index (GAI), plant area index (PAI) comparisons around moments of potential water related stress. ET map shows clear structures within field related to soil layer properties and root depth on the 13th of June. On the 30th of June, stress reaction in pigment and canopy structure can be seen with GAI and PAI.

4. Discussion

4.1. Thermal accuracy and impacts on spatial ET distribution

TSEB-PT's strong sensitivity to land surface temperature (LST) is well established (e.g., Hoffmann et al., 2016), but this study extends those findings using very-high-resolution UAV based thermal imagery under uniform crop cover. Uncorrected LST exhibited a significant underestimation, consistent with prior UAV studies (e.g., Kelly et al., 2019; Han et al., 2020; Wan et al., 2024; Tunca et al., 2023b; Liu et al., 2024). This bias led to systematic ET overestimation. While R^2 declined slightly after correction, the improved thermal realism enhanced physical consistency in ET estimates, particularly important for cumulative ET tracking and water balance assessments.

Thermal bias was most severe under high air temperature and wind speed, precisely when crops face peak transpiration demand and are most vulnerable to stress. This trend aligns with Sagan et al. (2019), who reported increased UAV TIR underestimation under warmer conditions. In our results, stressed areas showed amplified ET deviations with LST correction, indicating greater sensitivity to thermal accuracy. Underestimated LST muted ET suppression signals, reducing contrast between stressed and non-stressed zones and potentially misguiding irrigation responses. In addition, corrected LST sharpened spatial gradients in ET by enhancing energy balance contrast, particularly under dominant water or energy limitation conditions. This raised the standard deviation of ET values across the field and improved spatial differentiation of stress signals.

Despite onboard radiometric correction and a heated shutter for non-uniformity calibration, ground based reference targets remained essential for accurate LST and ET retrieval. When such targets are unavailable, alternate approaches like the Dual-Temperature Difference (DTD) variant of TSEB-PT can help, though in our case, DTD yielded only moderate improvements compared to ground-calibrated correction (results not shown).

4.2. Implications of LAI and f_c source and sensitivity to plant physiological properties

Both GAI and PAI served as effective LAI inputs for TSEB-PT during peak growth, when structural (PAI) and pigment based (GAI) indicators are closely aligned, yielding similar ET estimates. This is consistent with a prior one-source energy balance study showing LiDAR derived LAI can perform comparably to MS based LAI for ET estimations (Wei et al., 2023). However, few studies have examined how model performance shifts under stress or senescence, when canopy structure and function diverge.

Under these conditions, PAI remained high due to persistent canopy structure, which appears to contribute to higher ET overestimation. In contrast, GAI, which reflects pigment concentration and photosynthetic activity, captured

https://doi.org/10.5194/egusphere-2025-3919
Preprint. Discussion started: 21 August 2025

physiological decline and produced more conservative estimations that better aligned with EC ET. This effect was most pronounced in winter wheat, where structural density persisted even as transpiration decreased. While PAI and ground based ceptometer LAI showed better agreement in absolute values, especially in dense canopies where GAI saturates, neither completely captures declining physiological function. The results may indicate that GAI (functional LAI) better reflected actual transpiration capacity, which could explain the improved model performance when it was compared to PAI with f_g held constant at 1.

The automatic derivation of f_c from LAI in pyTSEB further complicates input selection. Because f_c governs the radiation partitioning between soil and vegetation, LAI input type influences both energy distribution and canopy resistance. GAI may underestimate shading in dense or senescent canopies, leading to lower f_c and thus lower modeled ET, not only due to higher canopy resistance but also reduced radiation allocated to the vegetation component. Conversely, PAI may overstate transpiration potential in structurally intact but functionally declining canopies. It is possible that while both LAI inputs perform similarly under non-stressed conditions, GAI offers better physiological realism during stress or senescence. Future implementations could benefit from testing the decoupling of f_c and LAI inputs, using structural data (PAI) for f_c and pigment-sensitive indices (GAI) for functional canopy resistance.

4.3. Role of f_g in differentiating functional transpiration from passive cooling

Distinguishing passive canopy cooling from actual transpiration is critical in dense canopies like winter wheat, where structure remains even as physiological function declines. Unlike eddy covariance systems, which directly measure vapor flux, TSEB-PT relies on LST as a proxy. Without accounting for canopy function, models may incorrectly attribute radiative cooling to transpiration. In this study, combining LiDAR based structural LAI (PAI) and MS derived pigment-sensitive LAI (GAI) enabled the use of f_g to scale transpiration according to physiological status, improving ET agreement with EC observations, particularly during early stress and senescence.

The f_g input proved effective even before visible signs of senescence (e.g. winter wheat), detecting early transpiration suppression due to stress. Despite its value, f_g is not required in TSEB-PT and is typically omitted. Comparable scaling is also lacking in models like SEBAL and METRIC, which treat vegetation as a single layer, an approach more suited to satellite-scale applications where such structural-functional distinctions are impractical. UAV platforms, however, not only offer the spatial resolution needed, but also provide new sensing capabilities, such as 3D structural mapping from LiDAR, that facilitate the integration of inputs like f_g.

UAV based ET studies that exclude the use of f_g in their TSEB-PT implementation further supports the importance of its inclusion. Gómez-Candón et al. (2021) reported overestimated ET (RMSE = 0.24 mm/h) in wheat without using f_g. This overestimation is more apparent in the later season with senescence. This overestimation is nearly identical to ours for winter wheat when we also excluded f_g. Similarly, Tunca et al. (2023a) observed overestimation in stressed sorghum and proposed manually adjusting the Priestley–Taylor coefficient (α), while our results show that incorporating f_g offers a more targeted and spatially dynamic alternative. Bozorgi et al. (2024) also identified

https://doi.org/10.5194/egusphere-2025-3919
Preprint. Discussion started: 21 August 2025

inaccurate assumptions about green canopy fraction as a source of TSEB bias, reinforcing the importance of function based scaling.

As shown in Figure 12, f_g influenced spatial ET variability more strongly than LAI type alone, highlighting its importance for accurate measurement. In winter wheat, this influence was limited, likely due to LAI saturation (>6), where additional canopy does not meaningfully alter radiation interception through f_c. In contrast, sugar beet and potato, with lower canopy density, showed greater f_g sensitivity. Given the strong link between f_c and f_g, improving f_c parameterization beyond the fixed extinction coefficient of the Beer–Lambert law used within the model could be valuable.

UAV LiDAR methods can now provide purely structural, high-resolution f_g estimates, avoiding pigment-related biases inherent in reflectance-only approaches (Chirouze et al., 2014). Unlike maximum NDVI methods, which fail to account for structural leaf loss during senescence, LiDAR derived f_g can explicitly track the green fraction relative to total canopy volume, potentially reducing biases in ET partitioning. These capabilities should be more widely integrated into UAV-based TSEB-PT workflows.

4.4 Future considerations with UAV TSEB model implementation

Satellite-based ET models have traditionally operated at coarse spatial scales, assuming simplified canopy structure and uniform land cover. In nearly all TSEB-PT applications, the LAI input is based on green LAI or GAI (Chirouze et al., 2014). Because f_c is often derived from LAI via the Beer–Lambert law in TSEB-PT (e.g. current pyTSEB), this can bias flux estimates in stressed or senescent crops by excluding nonfunctioning foliage that still shades the soil, leading to overestimation of soil heat flux (G) and soil-related flux components (Chirouze et al., 2014). While some studies have used plant area index (PAI) for f_c (Guzinski et al., 2014; Guzinski et al., 2020), these are rarely derived from purely structural metrics. As noted by Chirouze et al. (2014), f_c should reflect total canopy structure, whereas LAI should represent only the photosynthetically active portion. UAVs now enable direct, high-resolution measurements of both canopy structure and function. Leveraging structural LiDAR derived PAI for f_c (radiation partitioning) and functional multispectral derived GAI for LAI (canopy resistance) could enhance physiological realism in partitioning latent (LE_c) and sensible (H_c) heat fluxes, and warrants targeted testing.

Further sensor innovations could enhance the parameterization of ET models. For example, more detailed structural information from the entire canopy could be used to derive multi-layer GF profiles (Bates et al., 2022), supporting improved estimates of structural LAI. Additionally, LiDAR intensity, typically operating in the NIR range (Kim et al., 2009), has shown physiological associations with crop LAI (Hütt et al., 2022) and biomass (Montzka et al., 2023), offering potential as a dual-use input that integrates both structural and functional canopy traits into LAI and f_g estimates. UAV LiDAR can also contribute to guiding the parameterization of surface roughness as adjustments made to soil resistance coefficients has shown to be important (Li et al., 2019). Moreover, UAV-mounted radar systems, including synthetic aperture radar (SAR) and ground-penetrating radar (GPR), may provide novel pathways for assessing canopy or surface moisture conditions (Wu & Lambot et al., 2022), which are critical for accurate energy

https://doi.org/10.5194/egusphere-2025-3919
Preprint. Discussion started: 21 August 2025

flux partitioning. By leveraging the spatial precision and 3D reconstruction capabilities of UAV platforms, future research can further refine ET model inputs and improve accuracy across structurally complex and heterogeneous crop environments.

4.5. Practical impacts and considerations for farming practices

Physically based models like TSEB-PT offer major advantages over empirical or ML methods by simulating land–atmosphere energy exchanges without requiring extensive training data. In this study, TSEB-PT achieved accurate ET estimates using minimal ground measurements, just four control plots for LAI and h_c calibration and two thermal reference targets early in the season. Even fewer control points may suffice, shifting greater importance to UAV sensor quality and data type (e.g., LiDAR vs. MS). This highlights the operational value of TSEB-PT when paired with UAV platforms that can resolve fine-scale canopy and surface variability not captured by satellites.

The spatial and temporal resolution of UAVs allows ET to be mapped at actionable scales. In this study, UAV TIR-based ET estimations with TSEB-PT detected early signs of crop stress before they were visible in conventional means with MS or LiDAR based metrics. This capability enables the possibility of targeted, timely irrigation interventions. For instance, in the potato field, ET maps revealed under-irrigated zones just days after a hose reel event. In winter wheat, suppressed ET matched shallow gravel layers, flagging naturally water-limited zones that experienced early senescence. Such spatial detail would be difficult to detect through scouting or coarse-resolution remote sensing but is vital for optimizing yield and water use efficiency.

ET maps derived from UAV and TSEB can be interpolated to daily totals and integrated with rainfall and irrigation data to calculate crop water deficits or surpluses, supporting more precise irrigation scheduling. Several interpolation methods for converting instantaneous ET to daily values merit further investigation, particularly in relation to thermal sensor bias propagation, optimal overpass timing, and capturing the diurnal ET cycle through high-temporal UAV data. While this study focused on single-time observations aligned with EC fluxes, it highlights the potential of very-high-resolution UAV data and emerging sensor technologies to enhance spatial ET accuracy and inform future methodological advances.

5. Conclusion

This study demonstrates the effectiveness of integrating very-high-resolution UAV multi-sensor data with the TSEB-PT model for accurate, field-scale ET estimation across sugar beet, potato, and winter wheat over full growing seasons. With minimal ground calibration of UAV inputs, the model showed strong agreement with EC measurements, confirming its potential for operational use in precision irrigation and water management.

Among UAV derived inputs, TIR data was both the most influential and the most error-prone. Uncooled TIR sensors systematically underestimated LST under high-temperature and high-VPD conditions, leading to ET overestimation. Absolute LST correction using ground reference targets significantly improved both ET magnitude and spatial contrast, emphasizing the need for accurate thermal data. Vegetation inputs were also critical. While LiDAR derived

https://doi.org/10.5194/egusphere-2025-3919
Preprint. Discussion started: 21 August 2025

PAI and MS derived GAI performed similarly as LAI inputs for TSEB-PT during peak growth, results showed GAI more effectively reflected functional canopy decline under stress and senescence which may lead to a more accurate ET estimation during such periods. To further improve physiological relevance, we provided a dynamic input for f_g, derived from LiDAR-MS fusion with a GAI:PAI ratio. This enhanced ET accuracy and spatial variability, particularly in dense or senescing canopies, and proved valuable even before official senescence periods or visible signs of stress. Its inclusion could address overestimation issues seen in previous UAV based studies that omitted a functional canopy scaling parameter.

UAV platforms offer advantages over satellite systems by enabling fine-scale reconstruction of canopy structure using 3D LiDAR, along with thermal and spectral sensing for precise boundary layer characterization. These tools open new opportunities for near real-time ET mapping and water use assessment at actionable scales.

Key contributions of this study include:

- Demonstrating the robustness of TSEB-PT with UAV inputs and minimal ground calibration.
- Underscoring the importance of accurate TIR calibration, especially during heat stress.
- Clarifying divergence between structural (PAI) and functional (GAI) LAI inputs under stress.
- Proposing a LiDAR-MS fusion approach to estimate f_g for dynamic transpiration scaling.
- Establishing the value of f_g in TSEB-PT to improve ET accuracy across varying physiological states.
- Identifying crop-specific modeling challenges, especially in dense canopies like winter wheat.
- Showing the potential of UAV TIR based ET mapping to detect early stress to guide targeted irrigation.

Ultimately, this study highlights the value of combining UAV sensing with physically based models such as TSEB-PT for reliable, very-high-resolution ET monitoring. Future work should further explore the decoupling and type of inputs for f_c and LAI from advancing UAV sensors. In addition, further testing and improving dynamic LiDAR-MS based f_g integration across diverse cropping systems to enhance physiological realism and model scalability.

Appendix A: Description of the TSEB-PT model implementation

The Two-Source Energy Balance model with Priestley-Taylor formulation (TSEB-PT; Norman et al., 1995) was used to estimate surface energy fluxes, particularly latent heat flux (LE), by partitioning soil and canopy contributions based on radiometric surface temperature. The model was implemented in Python using the open-source pyTSEB package (Nieto et al., 2018). For more detailed description of TSEB, please refer to Norman et al. (1995) and W. P. Kustas & Norman (1999).

A1. Energy balance equations

$$R_n = LE + H + G \quad \text{(A1)}$$

Fluxes are partitioned into canopy and soil components:

https://doi.org/10.5194/egusphere-2025-3919
Preprint. Discussion started: 21 August 2025

$$R_{nc} = H_c + LE_c \quad \text{(A2)}$$

$$R_{ns} = H_s + LE_s + G \quad \text{(A3)}$$

Soil heat flux GGG is parameterized as a fraction of R_{ns}:

$$G = c_g R_{ns} \quad \text{(A4)}$$

Where c_g=0.35 is an empirical constant (Choudhury et al., 1987; Kustas & Daughtry, 1990).

A2. Sensible heat partitioning and air temperature

The total sensible heat flux H is calculated as:

$$H = H_c + H_s = \rho C_\rho \left[\frac{T_{ac} - T_c}{R_a}\right] = \rho C_\rho \left[\frac{T_c - T_{ac}}{R_x} + \frac{T_s - T_{ac}}{R_s}\right] \quad \text{(A5)}$$

Where T_{ac} = within-canopy air temperature (Kelvin); T_c and T_s = canopy and soil surface temperature components derived from UAV thermal imagery; ρ = air density (kg m^{-3}); C_ρ = heat capacity of the air at constant pressure (J/kg/K); R_a, R_s, and R_x = aerodynamic resistances (s m^{-1}).

The in-canopy air temperature is:

$$T_{AC} = \frac{\frac{T_A}{R_a} + \frac{T_C}{R_x} + \frac{T_S}{R_s}}{\frac{1}{R_a} + \frac{1}{R_x} + \frac{1}{R_s}} \quad \text{(A6)}$$

A3. Resistance parameterizations

Soil boundary layer resistance (Kustas & Norman, 1999):

$$R_s = \frac{1}{c(T_S - T_A)^{\frac{1}{3}} + bu_s} \quad \text{(A7)}$$

With the semi-empirical constants, b and c left at their default values. u_{su} represents wind speed near the soil surface.

Canopy resistance (Norman et al., 1995):

$$R_x = \frac{C'}{LAI}\left(\frac{S}{u_{d_0} + z_{0_m}}\right)^{\frac{1}{2}} \quad \text{(A8)}$$

Where C'($s^{1/2}$ m^{-1}) = 90 $s^{1/2}$ m^{-1} ; LAI = leaf area index estimated from either UAV multispectral GAI or LiDAR PAI; S (m) = characteristic leaf size; $u_{d_0} + z_{0_m}$ is the wind speed at the height reference height; $d_0 + z_{0_m}$ as d_0 is the zero-plane displacement height and z_{0_m} is the roughness length for moment estimated from UAV derived crop height.

https://doi.org/10.5194/egusphere-2025-3919
Preprint. Discussion started: 21 August 2025

$$R_a = \frac{\ln\left(\frac{z_T - d_0}{z_{0H}}\right) - \Psi_h\left(\frac{z_T - d_0}{L}\right) + \Psi_h\left(\frac{z_{0H}}{L}\right)}{k' u_*} \quad \text{(A9)}$$

z_T is the measurement heights for wind speed u (ms−1). d_0 is the zero-plane displacement height, z0H is the roughness length for momentum and heat transport with $z_{0_H} = z_{0_m}$ (−kB−1). The ψ (ζ) terms in Eqs. 7a and are the adiabatic correction factors for momentum. L being the Monin–Obukhov length (m).

A4. Radiometric temperature decomposition

The observed directional radiometric temperature T_{RAD} is decomposed as:

$$T_{RAD}(\theta) = [f_c(\theta) T_C^4 + (1 - f_c(\theta) T_S^4]^{1/4} \quad \text{(A10)}$$

Where $f_c(\theta)$ = vegetation fractional from the viewing angle (θ) calculated from UAV based multispectral.

A5. Priestley-Taylor approach to canopy transpiration

The initial estimate of LE_c uses the Priestley-Taylor formulation:

$$LE_c = \alpha_{PT} f_g \frac{\Delta}{\Delta + \gamma} R_{nc} \quad \text{(A11)}$$

Where α_{PT} = 1.26 (iteratively reduced if needed to achieve plausible solution LE_s >0; see W. Kustas & Anderson (2009)); f_g = fraction of green LAI derived from UAV based hybrid combination of multispectral and LiDAR data; Δ = slope of saturation vapor pressure curve (kPa K^{-1}); γ = psychrometric constant (kPa K^{-1}).

$$f_c(\theta) = 1 - exp\,[-k_{be}(\theta) LAI] \quad \text{(A12)}$$

with k_{be} being the extension coefficient of canopy with a leaf angle distribution defined by the Campbell (1990) parameter.

$$k_{be} = \frac{\sqrt{\chi^2 + tan^2\,\theta}}{\chi + 1.774\,(\chi + 1.182)^{-0.733}} \quad \text{(A13)}$$

Appendix B: Sensor derived metrics

B1. Green area index (multispectral)

$$FVC = \frac{NDVI - NDVI_s}{NDVI_v - NDVI_s} \quad \text{(B1)}$$

with $NDVI_s$ being the upper threshold for NDVI values representing soil pixels and $NDVI_v$ representing the upper threshold of healthy vegetation.

$$GAI = \frac{-log(1 - FVC)}{k(\theta)} \quad \text{(B2)}$$

https://doi.org/10.5194/egusphere-2025-3919
Preprint. Discussion started: 21 August 2025

$k(\theta)$ = extinction coefficient, parametrized using SunScan ceptometer LAI measurements. k was adjusted once between early and mid-late season and then held constant through senescence.

B2. Plant area index (LiDAR)

$$GF = \frac{n_{ground}}{n} \quad \text{(B3)}$$

n_{ground} = number of LiDAR returns classified as ground. n = total number of returns (ground + vegetation) in the pixel.

$$PAI = -\frac{cos\,(\underline{\theta})\,ln(GF)}{k} \quad \text{(B4)}$$

$\underline{\theta}$ = LiDAR scan angle ; GF = gap fraction from previous equation; k = extinction coefficient (same as above), adjusted once mid-season and then held constant.

B2. Crop height (LiDAR)

$$h_c = DSM_d - DTM_0 \quad \text{(B5)}$$

DSM_d = digital surface model from the crop canopy (per flight date); DTM_0 = digital terrain model from the bare soil pre-emergence flight.

Appendix C: Supplemental material

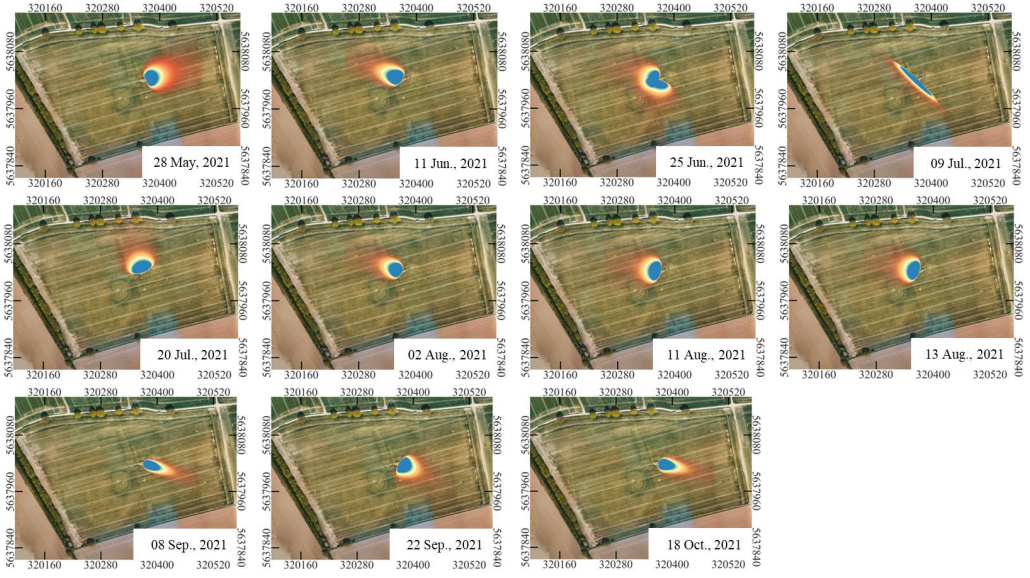

https://doi.org/10.5194/egusphere-2025-3919
Preprint. Discussion started: 21 August 2025

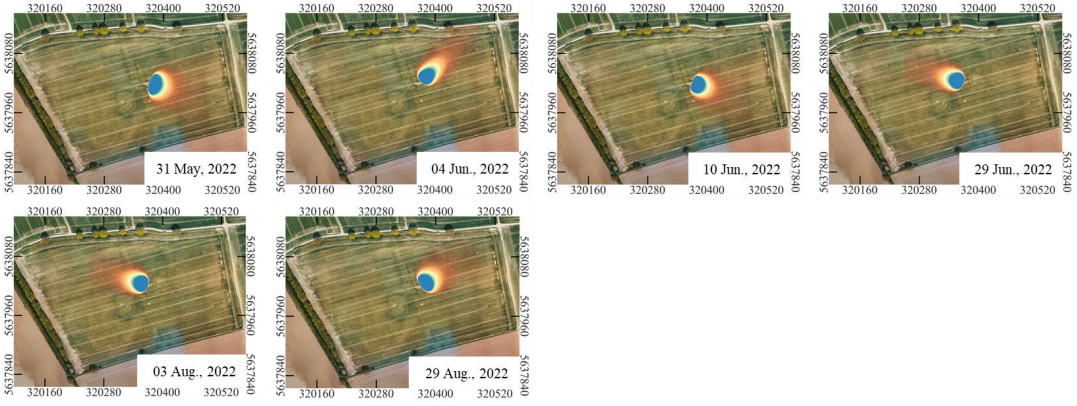

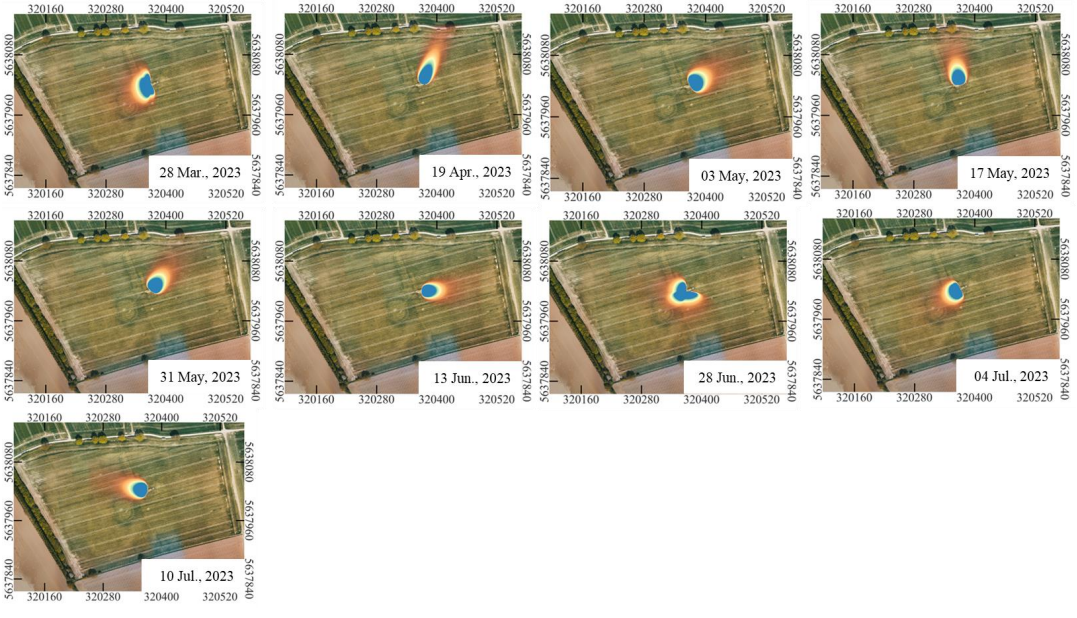

Figure C1: The estimated EC footprints for each TIR campaign flight time interval to be used to compare the TSEB-PT ET values within this spatial extent to the EC ET estimations.

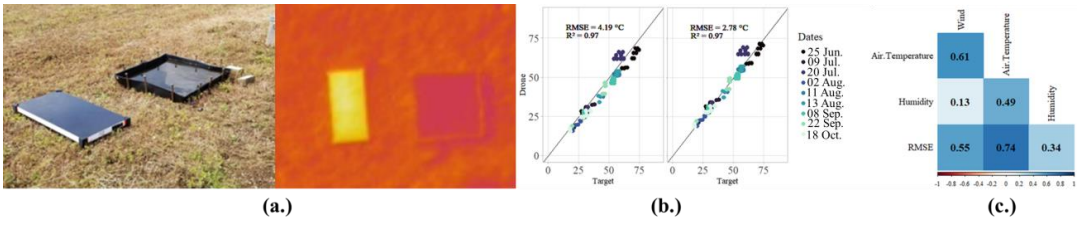

Figure C2 (a.) ground photo and aerial TIR view of the hot and cold temperature ground reference targets (b.)

https://doi.org/10.5194/egusphere-2025-3919
Preprint. Discussion started: 21 August 2025

pre-correction and post-correction graphed RMSE of TIR images in the 2021 season (c.) correlation of weather factors with RMSE.

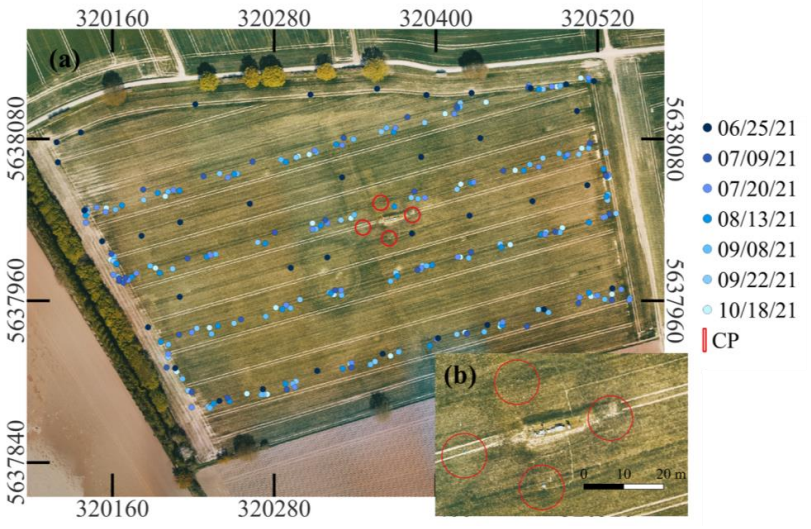

Figure C3: (Left) Location of continuous measurement plots (CP) around climate station in the middle of the experiment field site. (Right) Crop height measuring locations for the listed 2021 campaigns by color.

Table C1: The following TIR and MS collection dates with the relevant weather conditions during each flight that may have contributing factors on the accuracy of the observations.

Date	FLIR/MS Flights	LiDAR Flights	Start Time	End Time	Wind (m/s)	Air_Temp. (°C)	Humidity (%)	Wind_Direction (°)
5/28/2021	X	X	1310	1425	1.4	16.1	8.1	73
6/11/2021	X	X	1514	1619	2.3	25.9	11.9	295
6/25/2021	X	X	1228	1324	1.8	20.2	9.4	260
7/9/2021	X	X	1126	1233	1.2	17.8	13.1	304
7/20/2021	X		1328	1358	1.4	20.9	10	309
7/23/2021	X	X						
8/02/2021	X		1143	1212	0.9	15.4	10.6	299
8/11/2021	X		1400	1430	1.2	22.5	13.6	246
8/13/2021	X	X	1251	1328	2	22.5	12.7	287
9/08/2021	X		1328	1402	2.5	25.5	11.8	123
9/09/2021		X						
9/22/2021	X		1148	1227	0.9	16.7	8.6	133
9/28/2021		X						
10/18/2021	X		1400	1430	1.9	15.5	9.1	102
5/31/2022	X		1209	1251	0.8	15.3	8.2	102
6/04/2022	X	X	1447	1513	2.6	24.3	11.5	46
6/10/2022	X		1419	1448	1.3	22.1	11	226
6/29/2022	X	X	1512	1550	1.4	27.1	9.46	113

https://doi.org/10.5194/egusphere-2025-3919
Preprint. Discussion started: 21 August 2025

8/03/2022	X	X	1503	1533	1.9	31.7	10.7	292
8/29/2022	X	X	1508	1542	1.6	23.0	8.8	46
3/28/2023	X	X	1158	1235	0.9	6.6	3.8	250
4/19/2023	X	X	1323	1356	1.4	14.1	5.5	22
5/03/2023	X	X	1327	1341	1.2	14.3	6.5	55
5/17/2023	X	X	1350	1403	1.3	14.3	6.5	350
5/31/2023	X	X	1208	1240	1.5	22.2	9.4	38
6/13/2023	X	X	1257	1324	1.6	24.8	9.1	90
6/28/2023	X	X	1341	1410	1.4	20.5	11.5	225
7/04/2023	X		1243	1313	1.4	21.1	9.2	235
7/10/2023	X		1220	1251	1.6	24.7	11.3	283

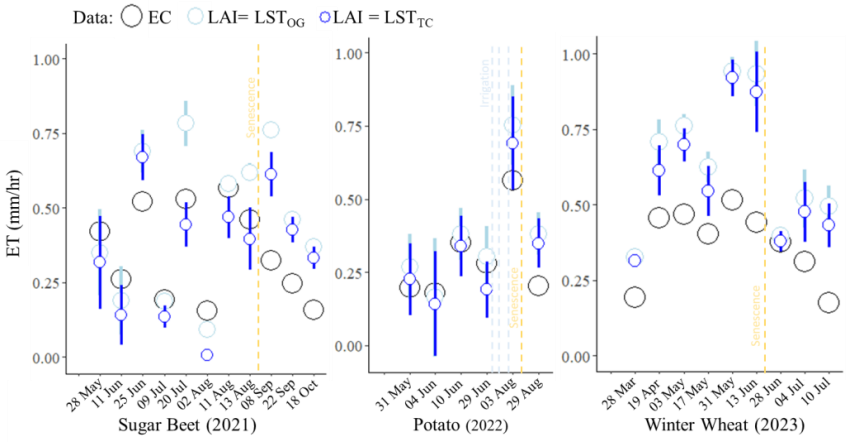

Figure C4: Field averages of the TSEB-PT ET estimations comparing the change between using LST$_{OG}$ and LST$_{TC}$ in comparisons to the EC ET estimations with (a) sugar beet in 2021 (b) potato in 2022 (c) winter wheat 2023.

https://doi.org/10.5194/egusphere-2025-3919
Preprint. Discussion started: 21 August 2025

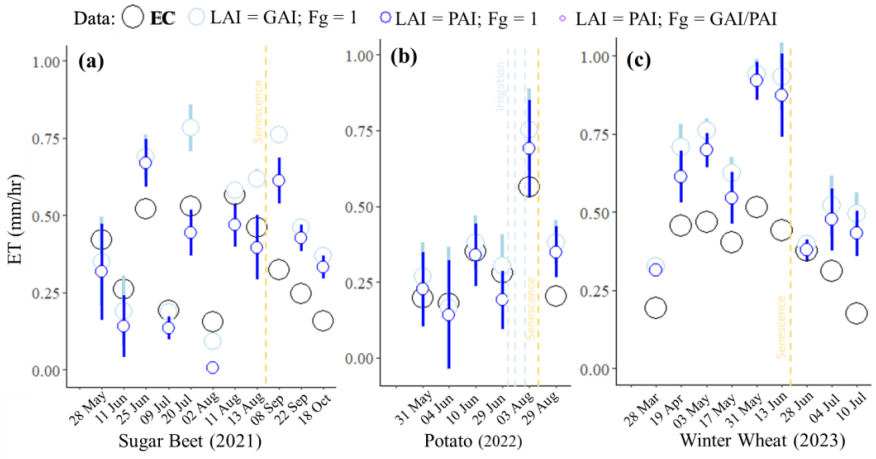

Figure C5: Field averages of the TSEB-PT ET estimations comparing the change between using GAI and PAI and the use of f_g in senescence stages in comparison to the EC ET estimations with (a) sugar beet in 2021 (b) potato in 2022 (c) winter wheat 2023.

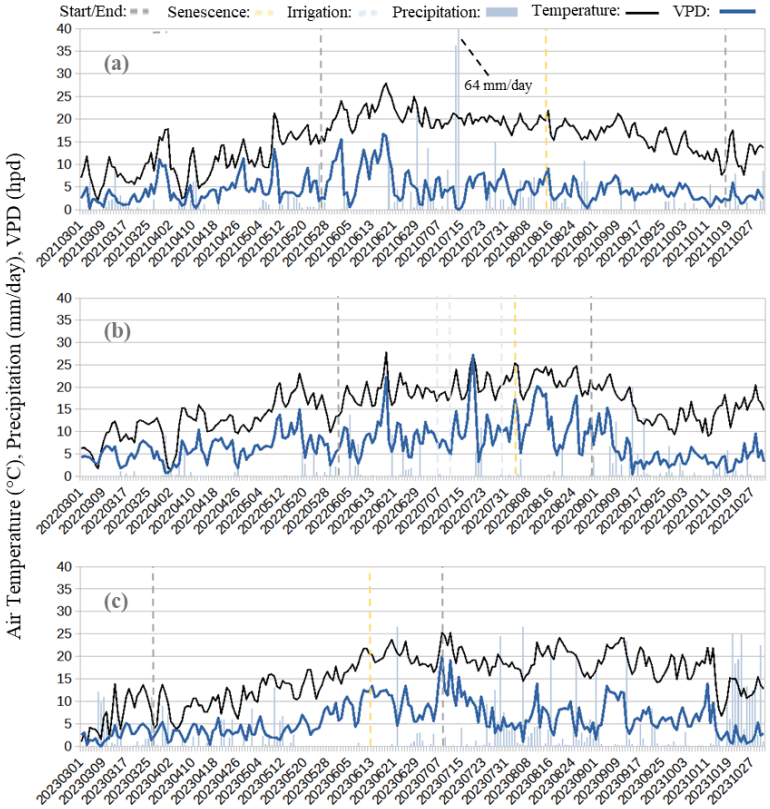

https://doi.org/10.5194/egusphere-2025-3919
Preprint. Discussion started: 21 August 2025

Figure C6: Daily air temperature, precipitation, and vapor pressure deficit (VPD) for the following years (a) 2021 (b) 2022 (c) 2023.

Code availability

Data will be available upon request.

Credit authorship contribution statement

Jordan Steven Bates: Writing – review & editing, Writing – original draft, Visualization, Software, Methodology, Investigation, Formal analysis, Conceptualization. **Carsten Montzka:** Writing – review & editing, Methodology, Investigation, Conceptualization. **Harry Vereecken:** Writing – review & editing, Methodology. **Francois Jonard:** Funding Acquisition,Writing – review & editing, Methodology, Investigation, Conceptualization, Supervision.

Declaration of competing interest

There is no conflict of interest.

Acknowledgments

The study was funded by the Deutsche Forschungsgemeinschaft (DFG, German Research Foundation) under Germany's Excellence Strategy—EXC 2070—390732324 and the Helmholtz Association Modular Observation Solutions for Earth Systems (MOSES) Initiative. Thank you to Marius Schmidt and his team for the LAI and crop height ground based validation measurements.

References

Ali, M., Montzka, C., Stadler, A., Menz, G., Thonfeld, F., & Vereecken, H. (2015). Estimation and Validation of RapidEye-Based Time-Series of Leaf Area Index for Winter Wheat in the Rur Catchment (Germany). *Remote Sensing*, *7*(3), Article 3.

Allen, R. G., Pereira, L. S., Raes, D., & Smith, M. (1998). FAO Irrigation and Drainage Paper No.56. *Food and Agriculture Organization*.

Amani, S., & Shafizadeh-Moghadam, H. (2023). A review of machine learning models and influential factors for estimating evapotranspiration using remote sensing and ground-based data. Agricultural Water Management, 284, 108324. DOI:10.1016/j.agwat.2023.108324

Amin, E., Verrelst, J., Rivera-Caicedo, J. P., Pipia, L., Ruiz-Verdú, A., & Moreno, J. (2021). Prototyping Sentinel-2 green LAI and brown LAI products for cropland monitoring. *Remote Sensing of Environment*, *255*, 112168.

Anderson, M. C., Kustas, W. P., Norman, J. M., Diak, G. T., Hain, C. R., Gao, F., Yang, Y., Knipper, K. R., Xue, J., Yang, Y., Crow, W. T., Holmes, T. R. H., Nieto, H., Guzinski, R., Otkin, J. A., Mecikalski, J. R., Cammalleri, C., Torres-Rua, A. T., Zhan, X., … Agam, N. (2024). A brief history of the thermal IR-based Two-Source Energy Balance (TSEB) model – diagnosing evapotranspiration from plant to global scales. *Agricultural and Forest Meteorology*, *350*, 109951.

Bates, J., Jonard, F., Bajracharya, R., Vereecken, H., & Montzka, C. (2022). Machine Learning with UAS LiDAR for Winter Wheat Biomass Estimations. *AGILE: GIScience Series*, *3*, 1–4.

https://doi.org/10.5194/egusphere-2025-3919
Preprint. Discussion started: 21 August 2025

731 Bates, J. S., Montzka, C., Schmidt, M., & Jonard, F. (2021). Estimating Canopy Density Parameters Time-Series for
732 Winter Wheat Using UAS Mounted LiDAR. *Remote Sensing*, *13*(4), Article 4.
733
734 Bellvert, J., Jofre-Ĉekalović, C., Pelechá, A., Mata, M., & Nieto, H. (2020). Feasibility of Using the Two-Source
735 Energy Balance Model (TSEB) with Sentinel-2 and Sentinel-3 Images to Analyze the Spatio-Temporal Variability of
736 Vine Water Status in a Vineyard. *Remote Sensing*, *12*(14), Article 14.
737
738 Bozorgi, M., Cristóbal, J., & Pàmies-Sans, M. (2024). Evaluating the Two-Source Energy Balance Model Using
739 MODIS Data for Estimating Evapotranspiration Time Series on a Regional Scale. Remote Sensing, 16(23), Article
740 23.
741
742 Brenner, C., Zeeman, M., Bernhardt, M., & Schulz, K. (2018). Estimation of evapotranspiration of temperate grassland
743 based on high-resolution thermal and visible range imagery from unmanned aerial systems. *International Journal of*
744 *Remote Sensing*, *39*(15–16), 5141–5174.
745
746 Brogi, C., Huisman, J. A., Herbst, M., Weihermüller, L., Klosterhalfen, A., Montzka, C., Reichenau, T. G., &
747 Vereecken, H. (2020). Simulation of spatial variability in crop leaf area index and yield using agroecosystem modeling
748 and geophysics-based quantitative soil information. *Vadose Zone Journal*, *19*(1), e20009.
749
750 Budzier, H., & Gerlach, G. (2015). Calibration of uncooled thermal infrared cameras. *Journal of Sensors and Sensor*
751 *Systems*, *4*(1), 187–197.
752
753 Bukowiecki, J., Rose, T., Ehlers, R., & Kage, H. (2020). High-Throughput Prediction of Whole Season Green Area
754 Index in Winter Wheat With an Airborne Multispectral Sensor. *Frontiers in Plant Science*, *10*.
755
756 Campbell, G. S. (1990). Derivation of an angle density function for canopies with ellipsoidal leaf angle distributions.
757 Agricultural and Forest Meteorology, 49(3), 173–176.
758
759 Cao, L., Liu, H., Fu, X., Zhang, Z., Shen, X., & Ruan, H. (2019). Comparison of UAV LiDAR and Digital Aerial
760 Photogrammetry Point Clouds for Estimating Forest Structural Attributes in Subtropical Planted Forests. *Forests*,
761 *10*(2), Article 2.
762
763 Chandel, A. K., Molaei, B., Khot, L. R., Peters, R. T., & Stöckle, C. O. (2020). High Resolution Geospatial
764 Evapotranspiration Mapping of Irrigated Field Crops Using Multispectral and Thermal Infrared Imagery with
765 METRIC Energy Balance Model. *Drones*, *4*(3), Article 3.
766
767 Chirouze, J., Boulet, G., Jarlan, L., Fieuzal, R., Rodriguez, J. C., Ezzahar, J., Er-Raki, S., Bigeard, G., Merlin, O.,
768 Garatuza-Payan, J., Watts, C., & Chehbouni, G. (2014). Intercomparison of four remote-sensing-based energy balance
769 methods to retrieve surface evapotranspiration and water stress of irrigated fields in semi-arid climate. Hydrology and
770 Earth System Sciences, 18(3), 1165–1188.
771
772 Choudhury, B. J., Idso, S. B., & Reginato, R. J. (1987). Analysis of an empirical model for soil heat flux under a
773 growing wheat crop for estimating evaporation by an infrared-temperature based energy balance equation.
774 *Agricultural and Forest Meteorology*, *39*(4), 283–297.
775
776 Colaizzi, P. (2016). Advances in a Two-Source Energy Balance Model: Partitioning of Evaporation and Transpiration
777 for Cotton. *Trans. ASABE*, *59*, 181–197.
778
779 Colaizzi, P. D., Agam, N., Tolk, J. A., Evett, S. R., & Howell, T. A. (2014). Two-Source Energy Balance Model to
780 Calculate E, T, and ET: Comparison of Priestley-Taylor and Penman-Monteith Formulations and Two Time Scaling
781 Methods. *Transactions of the ASABE*, 479–498.
782
783 de Lima, G. S. A., Ferreira, M. E., Sales, J. C., de Souza Passos, J., Maggiotto, S. R., Madari, B. E., de Melo Carvalho,
784 M. T., & de Almeida Machado, P. L. O. (2024). Evapotranspiration measurements in pasture, crops, and native
785 Brazilian Cerrado based on UAV-borne multispectral sensor. Environmental Monitoring and Assessment, 196(11),
786 1105

https://doi.org/10.5194/egusphere-2025-3919
Preprint. Discussion started: 21 August 2025

Derardja, B., Khadra, R., Abdelmoneim, A. A. A., El-Shirbeny, M. A., Valsamidis, T., De Pasquale, V., Deflorio, A. M., & Volden, E. (2024). Advancements in Remote Sensing for Evapotranspiration Estimation: A Comprehensive Review of Temperature-Based Models. Remote Sensing, 16(11), Article 11. https://doi.org/10.3390/rs16111927

Dou, X., & Yang, Y. (2018). Evapotranspiration estimation using four different machine learning approaches in different terrestrial ecosystems. Computers and Electronics in Agriculture, 148, 95–106. https://doi.org/10.1016/j.compag.2018.03.03

Elfarkh, J., Ezzahar, J., Er-Raki, S., Simonneaux, V., Ait Hssaine, B., Rachidi, S., Brut, A., Rivalland, V., Khabba, S., Chehbouni, A., & Jarlan, L. (2020). Multi-Scale Evaluation of the TSEB Model over a Complex Agricultural Landscape in Morocco. *Remote Sensing*, *12*(7), Article 7.

Ellsäßer, F., Röll, A., Stiegler, C., Hendrayanto, & Hölscher, D. (2020). Introducing QWaterModel, a QGIS plugin for predicting evapotranspiration from land surface temperatures. *Environmental Modelling & Software*, *130*, 104739.

Gao, R., Torres-Rua, A. F., Nieto, H., Zahn, E., Hipps, L., Kustas, W. P., Alsina, M. M., Bambach, N., Castro, S. J., Prueger, J. H., Alfieri, J., McKee, L. G., White, W. A., Gao, F., McElrone, A. J., Anderson, M., Knipper, K., Coopmans, C., Gowing, I., … Dokoozlian, N. (2023). ET Partitioning Assessment Using the TSEB Model and sUAS Information across California Central Valley Vineyards. *Remote Sensing*, *15*(3), 756.

Gao, R., Torres-Rua, A., Nassar, A., Alfieri, J., Aboutalebi, M., Hipps, L., Ortiz, N. B., McElrone, A. J., Coopmans, C., Kustas, W., White, W., McKee, L., Alsina, M. del M., Dokoozlian, N., Sanchez, L., Prueger, J. H., Nieto, H., & Agam, N. (2021). Evapotranspiration partitioning assessment using a machine-learning-based leaf area index and the two-source energy balance model with sUAV information. *Autonomous Air and Ground Sensing Systems for Agricultural Optimization and Phenotyping VI*, *11747*, 117470N.

García-Santos, V., Sánchez, J. M., & Cuxart, J. (2022). Evapotranspiration Acquired with Remote Sensing Thermal-Based Algorithms: A State-of-the-Art Review. *Remote Sensing*, *14*(14), Article 14.

Ghiat, I., Mackey, H. R., & Al-Ansari, T. (2021). A Review of Evapotranspiration Measurement Models, Techniques and Methods for Open and Closed Agricultural Field Applications. *Water*, *13*(18), Article 18.

Gogler, S., Madura, H., Krupiński, M., Bieszczad, G., & Sosnowski, T. (2014). Non-Uniformity Correction in Microbolometer Array with Temperature Influence Compensation. *Metrology and Measurement Systems; 2014; No 4; 709-718*.

Gómez-Candón, D., Bellvert, J., & Royo, C. (2021). Performance of the Two-Source Energy Balance (TSEB) Model as a Tool for Monitoring the Response of Durum Wheat to Drought by High-Throughput Field Phenotyping. *Frontiers in Plant Science*, *12*.

Guzinski, R., Nieto, H., Jensen, R., & Mendiguren, G. (2014). Remotely sensed land-surface energy fluxes at sub-field scale in heterogeneous agricultural landscape and coniferous plantation. Biogeosciences, 11(18), 5021–5046.

Guzinski, R., Nieto, H., Sandholt, I., & Karamitilios, G. (2020). Modelling High-Resolution Actual Evapotranspiration through Sentinel-2 and Sentinel-3 Data Fusion. Remote Sensing, 12(9), Article 9. https://doi.org/10.3390/rs12091433

Han, X., Thomasson, J. A., Swaminathan, V., Wang, T., Siegfried, J., Raman, R., Rajan, N., & Neely, H. (2020). Field-Based Calibration of Unmanned Aerial Vehicle Thermal Infrared Imagery with Temperature-Controlled References. *Sensors*, *20*(24), Article 24.

Hirschi, M., Michel, D., Lehner, I., & Seneviratne, S. I. (2017). A site-level comparison of lysimeter and eddy covariance flux measurements of evapotranspiration. Hydrology and Earth System Sciences, 21(3), 1809–1825. https://doi.org/10.5194/hess-21-1809-2017

https://doi.org/10.5194/egusphere-2025-3919
Preprint. Discussion started: 21 August 2025

Hoffmann, H., Nieto, H., Jensen, R., Guzinski, R., Zarco-Tejada, P., & Friborg, T. (2016). Estimating evaporation with thermal UAV data and two-source energy balance models. *Hydrology and Earth System Sciences*, *20*(2), 697–713.

Hunt Jr., E. R., & Daughtry, C. S. T. (2018). What good are unmanned aircraft systems for agricultural remote sensing and precision agriculture? *International Journal of Remote Sensing*, *39*(15–16), 5345–5376.

Hütt, C., Bolten, A., Hüging, H., & Bareth, G. (2022). UAV LiDAR Metrics for Monitoring Crop Height, Biomass and Nitrogen Uptake: A Case Study on a Winter Wheat Field Trial. PFG – Journal of Photogrammetry, Remote Sensing and Geoinformation Science, 91(2), 65–76. https://doi.org/10.1007/s41064-022-00228-6

Jaafar, H. H., Mourad, R. M., Kustas, W. P., & Anderson, M. C. (2022). A Global Implementation of Single- and Dual-Source Surface Energy Balance Models for Estimating Actual Evapotranspiration at 30-m Resolution Using Google Earth Engine. Water Resources Research, 58(11), e2022WR032800. https://doi.org/10.1029/2022WR032800

Jia, K., Li, Y., Liang, S., Wei, X., & Yao, Y. (2017). Combining Estimation of Green Vegetation Fraction in an Arid Region from Landsat 7 ETM+ Data. *Remote Sensing*, *9*(11), Article 11.

Kavya, B. M., & Mahadevaiah, T. (2024). Enhancing Estimation Of Evapotranspiration In Sugarcane Cultivation Using Lysimeter Data And Deep Learning Techniques. International Journal of Intelligent Systems and Applications in Engineering, 12(23s), Article 23s.

Kelly, J., Kljun, N., Olsson, P.-O., Mihai, L., Liljeblad, B., Weslien, P., Klemedtsson, L., & Eklundh, L. (2019). Challenges and Best Practices for Deriving Temperature Data from an Uncalibrated UAV Thermal Infrared Camera. *Remote Sensing*, *11*(5), Article 5.

Kim, S., McGaughey, R. J., Andersen, H.-E., & Schreuder, G. (2009). Tree species differentiation using intensity data derived from leaf-on and leaf-off airborne laser scanner data. Remote Sensing of Environment, 113(8), 1575–1586. https://doi.org/10.1016/j.rse.2009.03.017

Kljun, N., Calanca, P., Rotach, M. W., & Schmid, H. P. (2015). A simple two-dimensional parameterisation for Flux Footprint Prediction (FFP). *Geoscientific Model Development*, *8*(11), 3695–3713.

Kondo, J., & Ishida, S. (1997). Sensible Heat Flux from the Earth's Surface under Natural Convective Conditions. *Journal of the Atmospheric Sciences*, *54*(4), 498–509.

Korhonen, L., Korpela, I., Heiskanen, J., & Maltamo, M. (2011). Airborne discrete-return LIDAR data in the estimation of vertical canopy cover, angular canopy closure and leaf area index. *Remote Sensing of Environment*, *115*(4), 1065–1080.

Kustas, W., & Anderson, M. (2009). Advances in thermal infrared remote sensing for land surface modeling. *Agricultural and Forest Meteorology*, *149*(12), 2071–2081.

Kustas, W. P., & Daughtry, C. S. T. (1990). Estimation of the soil heat flux/net radiation ratio from spectral data. *Agricultural and Forest Meteorology*, *49*(3), 205–223.

Kustas, W. P., Nieto, H., Morillas, L., Anderson, M. C., Alfieri, J. G., Hipps, L. E., Villagarcía, L., Domingo, F., & Garcia, M. (2016). Revisiting the paper "Using radiometric surface temperature for surface energy flux estimation in Mediterranean drylands from a two-source perspective." *Remote Sensing of Environment*, *184*, 645–653.

Kustas, W. P., & Norman, J. M. (1999). Evaluation of soil and vegetation heat flux predictions using a simple two-source model with radiometric temperatures for partial canopy cover. *Agricultural and Forest Meteorology*, *94*(1), 13–29.

https://doi.org/10.5194/egusphere-2025-3919
Preprint. Discussion started: 21 August 2025

Li, Y., Kustas, W. P., Huang, C., Nieto, H., Haghighi, E., Anderson, M. C., Domingo, F., Garcia, M., & Scott, R. L. (2019). Evaluating Soil Resistance Formulations in Thermal-Based Two-Source Energy Balance (TSEB) Model: Implications for Heterogeneous Semiarid and Arid Regions. *Water Resources Research*, *55*(2), 1059–1078.

Liu, H., Song, W., Lv, J., Gui, R., Shi, Y., Lu, Y., Li, M., Chen, L., & Chen, X. (2024). Precise Drought Threshold Monitoring in Winter Wheat Using the Unmanned Aerial Vehicle Thermal Method. Remote Sensing, 16(4), Article 4. https://doi.org/10.3390/rs16040710

Liu, Y., Zhang, S., Zhang, J., Tang, L., & Bai, Y. (2021). Assessment and Comparison of Six Machine Learning Models in Estimating Evapotranspiration over Croplands Using Remote Sensing and Meteorological Factors. Remote Sensing, 13(19), Article 19. https://doi.org/10.3390/rs13193838

Liyew, C. M., Ferraris, S., Di Nardo, E., & Meo, R. (2025). A review of feature selection methods for actual evapotranspiration prediction. Artificial Intelligence Review, 58(10), 292. https://doi.org/10.1007/s10462-025-11298-4

Mendiguren, G., Koch, J., & Stisen, S. (2017). Spatial pattern evaluation of a calibrated national hydrological model – a remote-sensing-based diagnostic approach. *Hydrology and Earth System Sciences*, *21*(12), 5987–6005.

Mohan, M. M. P., Kanchirapuzha, R., & Varma, M. R. R. (2020). Review of approaches for the estimation of sensible heat flux in remote sensing-based evapotranspiration models. *Journal of Applied Remote Sensing*, *14*(4), 041501.

Mokhtari, A., Ahmadi, A., Daccache, A., & Drechsler, K. (2021). Actual Evapotranspiration from UAV Images: A Multi-Sensor Data Fusion Approach. *Remote Sensing*, *13*(12), Article 12.

Montzka, C., Donat, M., Raj, R., Welter, P., & Bates, J. S. (2023). Sensitivity of LiDAR Parameters to Aboveground Biomass in Winter Spelt. *Drones*, *7*(2), Article 2.

Nassar, A., Torres-Rua, A., Kustas, W., Nieto, H., McKee, M., Hipps, L., Stevens, D., Alfieri, J., Alsina, M., McKee, L., Coopmans, C., Sanchez, L., & Dokoozlian, N. (2020). Influence of Model Grid Size on the Estimation of Surface Fluxes Using the Two Source Energy Balance Model and sUAS Imagery in Vineyards. *Remote Sensing*, *12*, 342.

Nassar, A., Torres-Rua, A., Kustas, W., Alfieri, J., Hipps, L., Prueger, J., Nieto, H., Alsina, M. M., White, W., McKee, L., Coopmans, C., Sanchez, L., & Dokoozlian, N. (2021). Assessing Daily Evapotranspiration Methodologies from One-Time-of-Day sUAS and EC Information in the GRAPEX Project. *Remote Sensing*, *13*(15), Article 15.

Nassar, A., Torres-Rua, A., Hipps, L., Kustas, W., McKee, M., Stevens, D., Nieto, H., Keller, D., Gowing, I., & Coopmans, C. (2022). Using Remote Sensing to Estimate Scales of Spatial Heterogeneity to Analyze Evapotranspiration Modeling in a Natural Ecosystem. *Remote Sensing*, *14*(2), Article 2.

Nieto, H., Guzinski, R., & Kustas, W. P. (2018). pyTSEB: A python Two Source Energy Balance model for estimation of evapotranspiration with remote sensing data (Version 2.2) [Computer software]. https://doi.org/10.5281/zenodo.594732

Nieto, H., Kustas, W. P., Torres-Rúa, A., Alfieri, J. G., Gao, F., Anderson, M. C., White, W. A., Song, L., Alsina, M. del M., Prueger, J. H., McKee, M., Elarab, M., & McKee, L. G. (2019). Evaluation of TSEB turbulent fluxes using different methods for the retrieval of soil and canopy component temperatures from UAV thermal and multispectral imagery. *Irrigation Science*, *37*(3), 389–406.

Nieto, H., Alsina, M. M., Kustas, W. P., García-Tejera, O., Chen, F., Bambach, N., Gao, F., Alfieri, J. G., Hipps, L. E., Prueger, J. H., McKee, L. G., Zahn, E., Bou-Zeid, E., McElrone, A. J., Castro, S. J., & Dokoozlian, N. (2022). Evaluating different metrics from the thermal-based two-source energy balance model for monitoring grapevine water stress. Irrigation Science, 40(4), 697–713. https://doi.org/10.1007/s00271-022-00790-2

Niu, H., Hollenbeck, D., Zhao, T., Wang, D., & Chen, Y. (2020). Evapotranspiration Estimation with Small UAVs in Precision Agriculture. *Sensors*, *20*(22), 6427.

https://doi.org/10.5194/egusphere-2025-3919
Preprint. Discussion started: 21 August 2025

Niu, H., Zhao, T., Wang, D., & Chen, Y. (2019). Evapotranspiration Estimation with UAVs in Agriculture: A Review. *Preprints*.

Norman, J. M., Kustas, W. P., & Humes, K. S. (1995). Source approach for estimating soil and vegetation energy fluxes in observations of directional radiometric surface temperature. *Agricultural and Forest Meteorology*, *77*(3), 263–293.

Oguntunde, P., Olukunle, O. J., Fasinmirin, J., & Abiolu, O. A. (2012). Performance of the SunScan canopy analysis system in estimating leaf area index of maize. *Agricultural Engineering International: The CIGR Journal*.

Ortiz, M. S., Ducati, J. R., Espinoza, J., & Monteiro, C. (2019). Evapotranspiration Estimate Using Energy Balance Two Source Model With UAV Images: A Study in Vineyard. *American Journal of Engineering Research*, 11.

Park, S., Ryu, D., Fuentes, S., Chung, H., O'Connell, M., & Kim, J. (2021). Mapping Very-High-Resolution Evapotranspiration from Unmanned Aerial Vehicle (UAV) Imagery. *ISPRS International Journal of Geo-Information*, *10*(4), Article 4.

Pereira, A., & Pires, L. (2011). *Evapotranspiration and Water Management for Crop Production*.

Sagan, V., Maimaitijiang, M., Sidike, P., Eblimit, K., Peterson, K. T., Hartling, S., Esposito, F., Khanal, K., Newcomb, M., Pauli, D., Ward, R., Fritschi, F., Shakoor, N., & Mockler, T. (2019). UAV-Based High Resolution Thermal Imaging for Vegetation Monitoring, and Plant Phenotyping Using ICI 8640 P, FLIR Vue Pro R 640, and thermoMap Cameras. *Remote Sensing*, *11*(3), Article 3.

Tan, C.-W., Zhang, P.-P., Zhou, X.-X., Wang, Z.-X., Xu, Z.-Q., Mao, W., Li, W.-X., Huo, Z.-Y., Guo, W.-S., & Yun, F. (2020). Quantitative monitoring of leaf area index in wheat of different plant types by integrating NDVI and Beer-Lambert law. *Scientific Reports*, *10*(1), Article 1.

Tanner, C. B. (1963). Plant Temperatures. *Agronomy Journal*, *55*(2), 210–211.

Thorp, K. R., Hunsaker, D. J., & French, A. N. (2010). Assimilating Leaf Area Index Estimates from Remote Sensing into the Simulations of a Cropping Systems Model. *Transactions of the ASABE*, *53*(1), 251–262.

Tao, S., Song, L., Zhao, G., & Zhao, L. (2024). Simulation and Assessment of Daily Evapotranspiration in the Heihe River Basin over a Long Time Series Based on TSEB-SM. Remote Sensing, 16(3), Article 3. https://doi.org/10.3390/rs16030462

Tunca, E. (2023a). Evaluating the performance of the TSEB model for sorghum evapotranspiration estimation using time series UAV imagery. Irrigation Science, 42(5), 977–994. https://doi.org/10.1007/s00271-023-00887-2

Tunca, E., Köksal, E. S., & Taner, S. Ç. (2023b). Calibrating UAV thermal sensors using machine learning methods for improved accuracy in agricultural applications. Infrared Physics & Technology, 133, 104804. https://doi.org/10.1016/j.infrared.2023.104804

Virtue, J., Turner, D., Williams, G., Zeliadt, S., McCabe, M., & Lucieer, A. (2021). Thermal Sensor Calibration for Unmanned Aerial Systems Using an External Heated Shutter. *Drones*, *5*(4), Article 4.

Wan, Q., Smigaj, M., Brede, B., & Kooistra, L. (2024). Optimizing UAV-based uncooled thermal cameras in field conditions for precision agriculture. International Journal of Applied Earth Observation and Geoinformation, 134, 104184. https://doi.org/10.1016/j.jag.2024.104184

Wang, W., Zou, S., Luo, Z., Zhang, W., Chen, D., & Kong, J. (2014). Prediction of the Reference Evapotranspiration Using a Chaotic Approach. *The Scientific World Journal*, *2014*, e347625.

https://doi.org/10.5194/egusphere-2025-3919
Preprint. Discussion started: 21 August 2025

Wei, J., Dong, W., Liu, S., Song, L., Zhou, J., Xu, Z., Wang, Z., Xu, T., He, X., & Sun, J. (2023). Mapping super high resolution evapotranspiration in oasis-desert areas using UAV multi-sensor data. *Agricultural Water Management*, *287*, 108466.

Wu, K., & Lambot, S. (2022). Digital Soil Mapping Using Drone-Borne Ground-Penetrating Radar. In A. Di Mauro, A. Scozzari, & F. Soldovieri (Eds.), Instrumentation and Measurement Technologies for Water Cycle Management (pp. 417–436). Springer International Publishing. https://doi.org/10.1007/978-3-031-08262-7_17

Xia, T., Kustas, W. P., Anderson, M. C., Alfieri, J. G., Gao, F., McKee, L., Prueger, J. H., Geli, H. M. E., Neale, C. M. U., Sanchez, L., Alsina, M. M., & Wang, Z. (2016). Mapping evapotranspiration with high-resolution aircraft imagery over vineyards using one- and two-source modeling schemes. *Hydrology and Earth System Sciences*, *20*(4), 1523–1545.

Yang, Y. (2019). Remotely Sensed Evapotranspiration. In X. Li & H. Vereecken (Eds.), *Observation and Measurement of Ecohydrological Processes* (Vol. 2, pp. 155–200). Springer Berlin Heidelberg.

Yang, Y., Qiu, J., Zhang, R., Huang, S., Chen, S., Wang, H., Luo, J., & Fan, Y. (2018). Intercomparison of Three Two-Source Energy Balance Models for Partitioning Evaporation and Transpiration in Semiarid Climates. *Remote Sensing*, *10*(7), Article 7.

Yao, Y., Liang, S., Yu, J., Chen, J., Liu, S., Lin, Y., Fisher, J. B., McVicar, T. R., Cheng, J., Jia, K., Zhang, X., Xie, X., Jiang, B., & Sun, L. (2017). A simple temperature domain two-source model for estimating agricultural field surface energy fluxes from Landsat images: Simple ET Method. Journal of Geophysical Research: Atmospheres, 122(10), 5211–5236. https://doi.org/10.1002/2016JD026370

Yue, J., Guo, W., Yang, G., Zhou, C., Feng, H., & Qiao, H. (2021). Method for accurate multi-growth-stage estimation of fractional vegetation cover using unmanned aerial vehicle remote sensing. *Plant Methods*, *17*(1), 51.

Zhang, L., Zhang, H., Niu, Y., & Han, W. (2019). Mapping Maize Water Stress Based on UAV Multispectral Remote Sensing. *Remote Sensing*, *11*(6), Article 6.